POLITECNICO DI TORINO

Department of Mechanical and Aerospace Engineering

Master's Degree in Aerospace Engineering

On the effects of freestream turbulence on a small drone propeller aerodynamics and aeroacoustics

Supervisors:
Prof. Gioacchino Cafiero
Prof. Francesco Avallone
Prof. Daniele Ragni

Student:
Sara Montagner

Thesis in collaboration with the
Delft University of Technology

Academic Year 2023/2024

Abstract

This study investigates how turbulence affects the sound generated by propellers operating at low Reynolds number, combining both analytical and experimental approaches. Initially, incoming turbulence is analyzed using experimental data obtained via Particle Image Velocimetry (PIV) and Hot-Wire Anemometry (HWA). Additionally, oil-flow measurements were conducted. These experiments were conducted in the TU Delft A-tunnel, where acoustic measurements were also taken using a microphone arc.
Turbulence is generated by means of a grid, and its statistical properties, such as the turbulence intensity and the integral length scale, are examined. A comparison is made between these properties in scenarios with and without the propeller.
Subsequently, the turbulence statistics serve as input to an analytical noise-prediction model. This model predicts the power spectral density of the broadband noise emitted by the propeller when observed from a far-field position. Finally, the experimental spectrum obtained from microphone data is compared with the spectra predicted by the model.

Nomenclature

Acronyms

BPF: Blade Passing Frequency
CCD: Charge-Coupled Device
CMOS: Complementary Metal-Oxide Semiconductor
LSB: Laminar Separation Bubble
HWA: Hot Wire Anemometry
LE: Leading Edge
MIT: Massachusetts Institute of Technology
PIV: Particle Image Velocimetry
PSD: Power Spectral Density
PWL: Sound Power Level
RDT: Rapid Distortion Theory
RPM: Revolution Per Minute
SPL: Sound Pressure Level
UAV: Unmanned Aerial Vehicles
VTOL: Vertical Take-Off and Landing

Greek Symbols

α: out of plane angle of rotor blade
α_{20}: hot wire sensor TCR
β_{max}: maximum twist angle of the propeller
γ: azimuthal blade angle
$\Gamma(.)$: Gamma function
ε: average rate of dissipation of turbulence kinetic energy per unit mass
η: Kolmogorov micro scale
θ: angle of observer from upstream rotor axis
σ: standard deviation
σ^2: $x^2 + \beta^2(y^2 + z^2)$
ϕ_{ww}: turbulence spectrum
ν: kinematic viscosity
ρ_0: air density
ω: radian frequency
ω_0: Doppler-shifted radian frequency

Ω: angular frequency of the blade

Roman Symbols

a: radius of the cylinder
b: airfoil semi-chord
B: number of blades
c_0: sound speed
c_{max}: maximum value of the chord of the propeller
$C.R.$: contraction ratio
C_Q: torque coefficient
C_T: trust coefficient
d: width of the rods of the grid
D: diameter of the propeller
$E[\dots]$: expected value operator
E^*: Fresnel integral
$E(k)$: energy spectrum
f: frequency
g: airfoil response function
G: mesh size of the grid
I: turbulent intensity
J: advance ratio
k: wavenumber
k_e: wavenumber of the largest eddies
k_x, k_y: x and y wavenumbers
$l_y(\omega)$: spanwise coherence length
L: turbulence integral length scale
L_{ij}^m: integral length scale along m-direction
L_{uu}: integral length scale for the streamwise velocity component
$\mathscr{L}$: effective lift
m: direction along which the correlation is calculated
M: Mach number
M_b: chord-wise Mach number of the blade
M_f: flight Mach number in rotor plane
M_t: Mach number of the blade segment relative to the rotor hub
M_z: flow Mach number along the rotor axis
n: propeller rotational frequency
ΔP_T: total pressure jump
r: position along the blade of the propeller
r_e: distance from observer to retarded source
R: radius of the propeller
R_{20}: hot wire sensor resistance at 20 °C
$R_{ij}(m)$: spatial correlation function along m-direction
R_L: hot wire leads resistance
Re: Reynolds number

Re_d: Reynolds number related to the grid
S_{PP}: far-field PSD
S_{QQ}: cross-PSD
$S_{ww}(\omega)$: PSD of the vertical velocity fluctuations
Te: time between emission and reception of sound
$\bar{u}$: mean velocity of the flow
u': fluctuating velocity component
u'_{rms}: root mean square of the turbulent velocity fluctuation
U_∞: freestream velocity
U_1: velocity of the flow before the contraction
U_2: velocity of the flow after the contraction
$\mathbf{x}_0$: vector from rotor hub to observer
$\mathbf{x}_p$: present source position
$\mathbf{x}_s$: vector from rotor hub to retarded source position

Contents

List of Figures

List of Tables

1

Introduction

1.1 Background

Unmanned aerial vehicles (UAVs), often referred to as drones, rose in popularity during the 1990s thanks to progress in control technology, electronics, and wireless control alternatives. These days, they find extensive use across commercial, military, and industrial sectors, including agriculture, rescue operations, observational tasks, reconnaissance, and cargo transport.
At present, propellers are the primary propulsion system utilized in these vehicles. This choice is due to their ability to provide the necessary thrust-to-weight ratio for hovering and executing swift maneuvers, especially in confined spaces close to obstacles.
The rapid growth of the drone market is intricately tied to efforts aimed at reducing rotor noise. Propeller noise stands out as a major concern, limiting the widespread adoption of UAVs in everyday activities. People find UAV noise more bothersome compared to noise from road vehicles or other modes of transportation [7]. This has led to a significant focus on propeller acoustics in recent decades, emphasizing the importance of propeller noise reduction and sparking engineering endeavors worldwide.

1.2 Report structure

The first part of this work introduces turbulence and its characteristics. The aerodynamics of propellers operating at low Reynolds numbers is then briefly introduced, and a study of the relationship between propeller and inflow turbulence is reported from the aerodynamic and propeller-generated noise points of view.
The third chapter presents the analytical model used for noise prediction, while the following chapter presents the different experimental setups carried out during the experimental campaign. These setups include different experimental techniques, including Stereo Particle Image Velocimetry (PIV), acoustic measurements, hot wire anemometry (HWA) and oil flow visualisation. The results of the experiments in terms of turbulence characterisation are then presented. Finally, a comparison is made between the noise spectra obtained from the predictive model and the acoustic experimental data, providing an insight into the accuracy of the model in predicting the noise generated by propellers operating at low Reynolds numbers.

2

Literature review

2.1 Turbulence

Almost all flows occurring in nature and in engineering applications are turbulent such as the majority of terrestrial atmospheric and oceanic currents, the rapid flow of fluid around a bluff body or airfoil, the motion that characterizes the dispersion of pollutants in air and many others.
To date, a fully satisfactory definition of turbulent flows has not been found, but we can describe turbulence by listing its main characteristics.

- Turbulence is a random process. A variable, which as a result of experimentation under defined conditions, can assume any one of a number of possible numerical values which would be impossible to predict in advance, is called a *random variable* [12]. Any variable occurring in a turbulent flow, such as velocity, pressure or temperature, is a random function of position $\mathbf{x}$ and time t. The irregularity or randomness of all flow parameters makes the deterministic approach to turbulence problems impossible; instead one relies on statistical methods since the only reproducible properties of a turbulent flow are the statistical ones.

- Turbulence appears when inertial forces prevail over viscosity forces in a flow, which implies that the Reynolds number measuring the relative strength of these two forces must exceed a certain threshold [4].

- Turbulent flow is space and time dependent with a very large number of spatial degrees of freedom and it's strongly nonlinear: a small perturbation of the initial conditions can cause a large and unpredictable change in the velocity field of the fluid.

- A turbulent flow contains a wide range of different scales that coexist. In particular, the smaller scales, at which energy dissipation takes place, are generated from the larger ones through an energy transfer phenomenon called energy cascade.

- Turbulent flows are rotational and intrinsically three-dimensional. Turbulent flow can be considered to consist of the mean motion superimposed on which are randomly varying components of velocity in all three directions. A similar statement can be made about other variables [12].

- Turbulence is highly diffusive in nature and this causes rapid mixing and increased rates of momentum, heat and mass transfer.

2.1.1 Energy cascade

In order to understand the mechanism of the energy cascade it is important to give the definition of eddy. An eddy is a turbulent motion, localized within a region of size l, that is at least moderately coherent over this region. During its motion an eddy can change its shape or stretch, and rotate or break into more eddies [12].
As previously said a turbulent flow contains a wide range of different scales that coexist so the turbulence can be considered to be composed of eddies of different scales. Bigger eddies are characterized by the length-scale L. The Reynolds number of these eddies is large and the effects of viscosity are negligible. These eddies are unstable and break-up, transferring their energy to somewhat smaller eddies. These smaller eddies undergo similar break-up process transferring their energy to yet smaller energy.
This process, first introduced by Richardson in 1922, is called *energy cascade* and it's driven by inertial forces. The process continues until Reynolds number is sufficiently small that viscosity becomes important and the dissipation of the turbulent kinetic energy occurs. When the size of the eddies is small enough such that the Reynolds number becomes almost unitary the viscosity becomes predominant and the turbulent energy is dissipated into heat. The size of the smaller eddies depends on the Reynolds number of the flow and their length-scale η is called dissipation or Kolmogorov length-scale. The size of this scale (η) depends on the rate of dissipation ε and on the kinematic viscosity ν. In particular:

$$\eta = \left(\frac{\nu^3}{\varepsilon}\right)^{1/4} \tag{2.1}$$

2.1.2 Statistical approach and reference quantities

From a mathematical point of view we can represents a turbulent flow as a mean flow plus a random, fluctuating component of motion:

$$\mathbf{u}(\mathbf{x}, t) = \bar{\mathbf{u}}(\mathbf{x}) + \mathbf{u}'(\mathbf{x}, t) \tag{2.2}$$

where, at any instant, u' consists of a random collection of eddies [9].
Since the turbulent fluctuations are caused by the generation, convection, diffusion and dissipation of eddies, they vary from time to time and from place to place in a very complex and random manner. Therefore, a deterministic approach is unlikely to yield satisfactory result and for this reason the statistical approach is used.
A random flow variable, such as velocity u, at a given position and time, may be characterized by its probability density function (PDF). In a turbulent flow, u will take on different values in repeated experiments; the probability density function, $P(u)$, is such that $P(u)du$ is the probability of u lying between u and $u + du$. Since u must always take on some value:

$$\int_{-\infty}^{+\infty} P(u)du = 1 \tag{2.3}$$

The mean value of u can be calculated from $P(u)$:

$$\bar{u} = \int_{-\infty}^{+\infty} u \cdot P(u) du \tag{2.4}$$

Another important parameter to consider is the standard deviation, σ, of u that is a measure of the the magnitude of the random fluctuations.

$$\sigma = \sqrt{\overline{(u - \bar{u})^2}} \tag{2.5}$$

Length scales

As previously said into a turbulent flow exist a huge spectrum of eddy sizes. We can therefore identify the two characteristic length scales that are used to describe turbulence from a statistical point of view.
The first one is the integral scale L that represents the linear dimension of the largest eddies to which a high kinetic energy content is associated. The integral scale is defined as:

$$L_{ij}^{m} = \int_{0}^{\infty} R_{ij}(m) dm \tag{2.6}$$

where *R(m)* is the spatial correlation function, m is the direction along which the correlation is calculated and i and j are the quantities of the variables involved in the computation in the two points considered. The correlation function describes the statistical spatial dependence of two variables and it is defined as follows:

$$R_{ij}(m) = \frac{\overline{i(m)j(m + dm)}}{\sigma_i \sigma_j} \tag{2.7}$$

The other important scale of the turbulence is the Kolmogorov micro-scale, or dissipative scale, η that represent the size of the smaller eddies. Vortices of this size are those at which the dissipation of turbulent kinetic energy into heat occurs. The viscous dissipation is controlled by the rate of dissipation ε and by the kinematic viscosity ν, as seen in eq. 2.8.
The relationship between large and small scales depends on the Reynolds number based on the large-scale eddies through the following equation:

$$\frac{\eta}{L} = \left(\frac{UL}{\nu}\right)^{3/4} = Re^{3/4} \tag{2.8}$$

The higher the Reynolds number, the finer the small scale structures and the greater the scale separation between L and η [9].
The following picture, from Pope [24], shows the signal spectrum for various Reynolds numbers. We can see that as the Reynolds number increases, the inertial region expands.

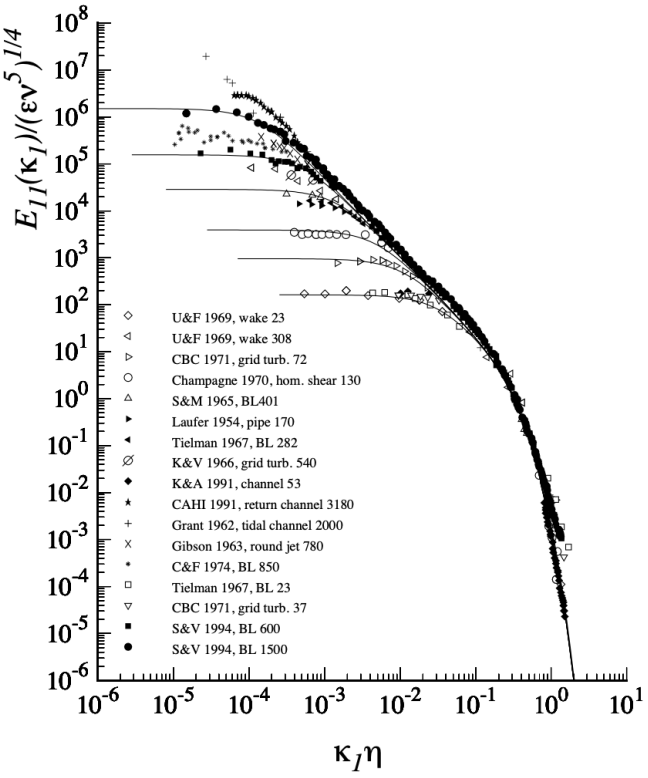

Figure 2.1: Measurement of one-dimensional longitudinal velocity spectra (symbols) and model spectra (lines) for $Re_\lambda = 30$, 70, 130, 300, 600 and 1300. The experimental data are taken from Saddoughi and Veeravalli (1994) where references to the different experiments are given. For each experiment, the final number in the key is the value of Re_λ. [24]

Intensity

Another important quantity useful to characterize the turbulence is its intensity, I. It represents the intensity of the velocity fluctuations with respect to the value of the mean flow velocity and it's defined ad follows:

$$I = \frac{u'_{rms}}{U_\infty} \tag{2.9}$$

where u'_{rms} is the root mean square of the turbulent velocity fluctuation.

$$u'_{rms} = \sqrt{\frac{u'^2 + v'^2 + w'^2}{3}} \tag{2.10}$$

2.1.3 Homogeneous and isotropic turbulence

An homogeneous and isotropic turbulence is a turbulence of which the statistical properties do not vary with position and have no preferred direction [30].
Considering the hypothesis oh homogeneous and isotropic turbulence, Von Karman [33] proposed a semi-empirical relationship for the energy spectrum function $E(k)$, which indicates the distribution of energy over different length scales. His relationship for $E(k)$ considers the Kolmogorov dependence in the inertial subrange ($k^{-5/3}$) and the dependence for small wavenumbers (k^4). The Von Karman energy spectrum function is given as [27]:

$$E(k) = \frac{55}{9\sqrt{\pi}} \frac{\Gamma(5/6)\overline{u'^2}}{\Gamma(1/3)k_e} \frac{(k/k_e)^4}{[1+(k/k_e)^2]^{17/6}} \tag{2.11}$$

where k_e is the wavenumber scale of the largest eddies

$$k_e = \frac{\sqrt{\pi}}{L} \frac{\Gamma(5/6)}{\Gamma(1/3)} \tag{2.12}$$

The input parameters to calculate $E(k)$ are the turbulence intensity and the integral length scale, so they determine the shape of the energy function.
An increase in the turbulence intensity produces an overall increase in energy for all wavenumbers, while decreasing the integral length scale increases the energy contained in the range related to the higher wavenumbers.

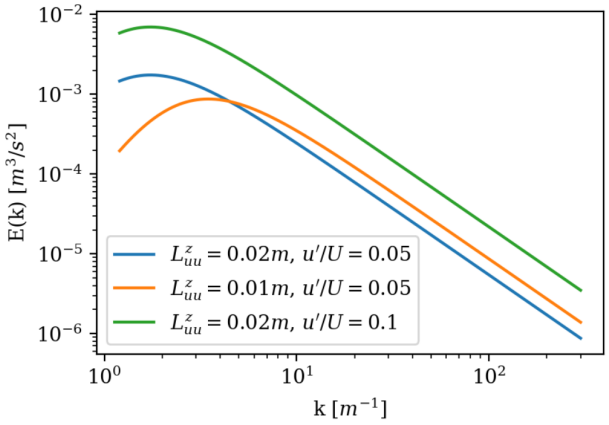

Figure 2.2: Von Karman energy spectrum for various combination of length scale and intensity as a function of turbulence wavenumber k [32]. Mean flow velocity $U_\infty = 10m/s$.

2.2 Grid turbulence

One of the simplest and most efficient methods of generating quite isotropic and homogeneous turbulence is by means of a grid placed normally with respect to the direction of mean flow. Immediately downstream of the grid, the flow is strongly inhomogeneous, but at a certain distance the flow is well mixed and the turbulence becomes nearly

homogeneous. We can consider that the conditions of homogeneous and isotropic turbulence are reached at a distance of about 10 mesh sizes (G) downstream the grid [25]. The characteristics of turbulence generated by means of a grid are strongly influenced by the geometric characteristics of the grid itself. In particular, the mesh size G determines the distance downstream of the grid at which the turbulence can be considered homogeneous and isotropic, while the width of the rods d has a strong impact on the length scale and the turbulence intensity.

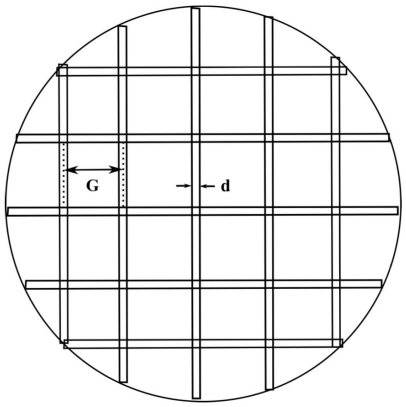

Figure 2.3: Grid pattern.

For high Reynolds number flows, that is above those where viscous effects are significant, the turbulent downstream intensity follows the next equations [25]:

$$\begin{cases} Tu = C\left(\frac{x}{d}\right)^{-5/7} \\ Tv = CD\left(\frac{x}{d}\right)^{-5/7} \end{cases} \tag{2.13}$$

where $Tu = \frac{\sqrt{u'^2}}{U_\infty}$ and $Tv = \frac{\sqrt{v'^2}}{U_\infty}$ are the streamwise and the normal components of the turbulence intensity. Then, x is the distance downstream of the grid and d is the representative grid dimension (i.e. the width of the rods). The "constants" C and D are functions of the type and the geometry of the grid. A similar expression can be found for the third component.

Now considering homogeneous and isotropic turbulence, such as the one generated downstream of a grid, it's also possible to derive a relationship between the microscale and the turbulence decay rate. This leads to write the following relations for the streamwise and the normal components respectively:

$$\left(\frac{\eta_x}{d}\right)^2 = \frac{14F(x/d)}{Re_d} \tag{2.14}$$

$$\left(\frac{\eta_y}{d}\right)^2 = \frac{7G(x/d)}{Re_d} \tag{2.15}$$

where $Re_d = \frac{U_\infty d}{\nu}$ is the Reynolds number of the grid, while F and G are constants. Assuming then that the integral scale grow at a rate which is proportional to the grow

rate of the micro scale it's possible to write the following relationships:

$$\frac{L_x}{d} = I\left(\frac{x}{d}\right)^{1/2} \tag{2.16}$$

$$\frac{L_y}{d} = \frac{IJ}{2}\left(\frac{x}{d}\right)^{1/2} \tag{2.17}$$

where I and J are constants.

2.3 Turbulence distortion

Modeling turbulence distortion is of fundamental importance because this aspect has a strong impact on turbulence ingestion noise.
We can identify two causes of turbulence distortion: the first is related to streamtube contraction, while the second is related to the interaction of turbulent flow with the airfoil.

2.3.1 Streamtube contraction

Prandtl was the first to analyze what happened to a turbulent flow when it accelerated due to the contraction of the streamtube. He discovered that a sharp decrease in the cross-sectional area of a pipe with a consequent increase in the mean speed smooths out the flow irregularities.
The main assumption of the Prandtl's theory is to consider vorticity as the main variable in a turbulent flow, neglecting the effect of the walls. This means that, in an incompressible fluid, the velocity changes can only be produced by vorticity. In this way it's possible to determine the effect of contraction on free-stream turbulence by considering its effect on vorticity [31].
Another important hypothesis of the Prandtl's theory is that the velocity fluctuations in the streamwise (x) direction are mainly caused by the vortex filaments lying perpendicular to that direction. The same reasoning applies for the other directions. Prandtl discovered that, as the flow goes through the contraction, the vortex filaments in the streamwise direction are elongated by a factor CR, while those in the y and z directions are contracted by a factor $\sqrt{CR}$. The factor CR is the ratio between the two velocities after and before the contraction [31].

$$CR = \frac{U_2}{U_1} \tag{2.18}$$

Neglecting viscosity we can say that the product of the angular velocity and the cross-sectional area of the vortex filament has to remain constant. It is therefore possible to write this relationships:

$$\frac{u_2}{u_1} = \frac{1}{CR} \tag{2.19}$$

$$\frac{v_2}{v_1} = \frac{w_2}{w_1} = \sqrt{CR} \tag{2.20}$$

We expect that, as a flow goes through a contraction, the streamwise component of turbulence fluctuations decreases while the normal components increase.

The experiments conducted by Uberoi [31] confirmed the behaviour predicted by Prandtl. His experiments led to show the behaviour of the turbulence components for different contraction ratios (4:1 and 9:1). The results are reported in figure 2.5 and show that, in accordance with Prandtl's prediction, $\overline{u^2}$ decreases and $\overline{v^2}$ increases as the flow accelerates through the contraction.

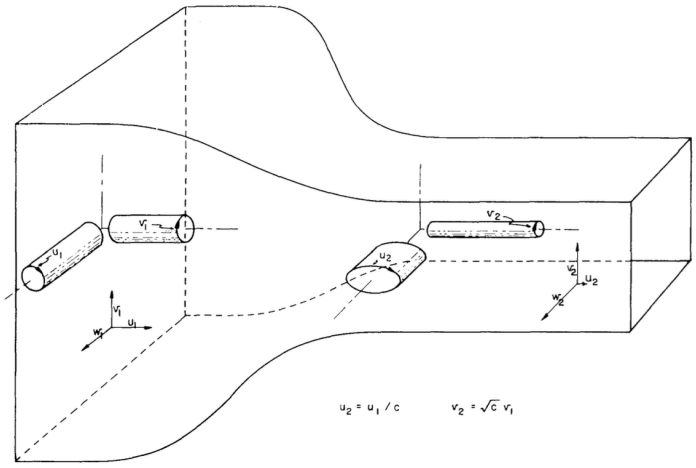

Figure 2.4: Representation of Prandtl's semi-quantitative theory where $c = CR$

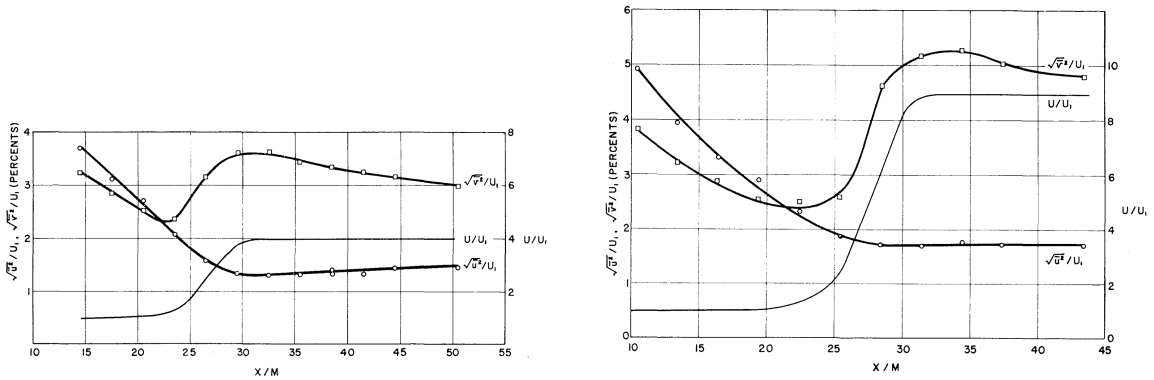

(a) Contraction ratio 4:1

(b) Contraction ratio 9:1

Figure 2.5: Effect of two different contraction ratio on turbulent components

2.3.2 Interaction with the airfoil

The second cause of turbulence distortion is the interaction of a turbulent inflow with an airfoil. Since the latter is a thick body, when the flow impacts on it a distortion of the flow field occurs.
In 1973, Hunt formulated the rapid distortion theory (RDT) to model the changes of the turbulent velocity field when it interacts with a bluff body. This theory assumes that the time taken for a fluid particle to pass through the zone in which the mean velocity changes is very much less than the time taken for the turbulence to change of its own accord owing to its own viscous and nonlinear inertial forces [16]. Moreover,

the velocity fluctuations of the incoming inflow are supposed to be small compared with the free-stream velocity. In his work, Hunt carried out a wavenumber analysis to compute the homogeneous turbulent flow past a circular cylinder. An important result of the theory is that it illuminates and distinguishes between the governing physical processes of distortion of the turbulence by the mean flow: the direct "blocking" of the turbulence by the body, and concentration of vortex lines at the body's surface [16]. The prevalence of one distortion mechanism over the other depends on the ratio L_x/a, where L_x is the streamwise integral length scale of the turbulence and a is the radius of the cylinder. In particular:

- For $L_x/a \gg 1$ the prevailing distortion mechanism is due to the blockage imposed by the presence of the body, which causes a momentum transfer between the streamwise and the upwash velocity components of a fluid element approaching the cylinder along the streamwise stagnation streamline. As a result the streamwise velocity fluctuations decrease near the surface while the upwash ones increase [23].
- For $L_x/a \ll 1$ the dominant distortion mechanism is determined by the deformation of the vorticity field due to the deflection of the streamlines upstream and around the body. In this case we can observe that the streamwise and spanwise velocity fluctuations increase while the upwash ones decrease [23].

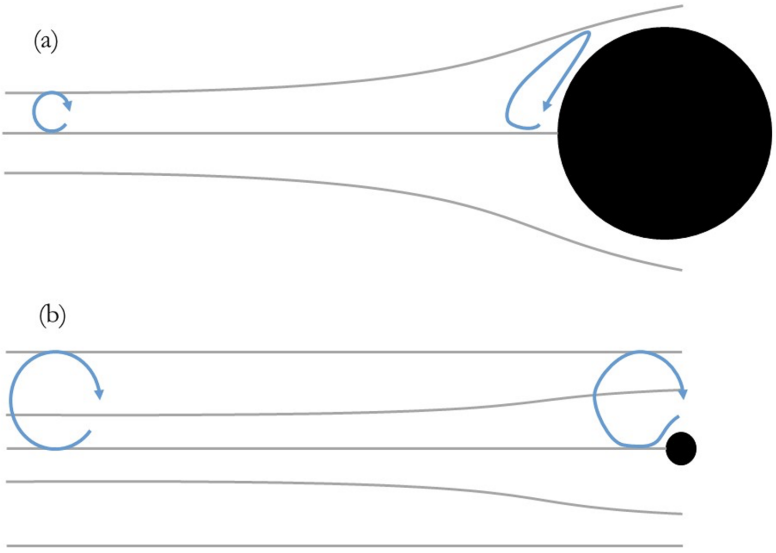

Figure 2.6: Qualitative representation of the two distortion mechanisms: (a) for $L_x/a \ll 1$ and (b) for $L_x/a \gg 1$.

This theory has been developed to model the interaction of incoming weak turbulence with a bluff body and subject to rapid distortion. Mish and Devenport [18] provided that it can be extended to airfoil if the distortion occurring near the leading edge is considered and the airfoil is seen as a cylinder with radius equal to the leading-edge radius.

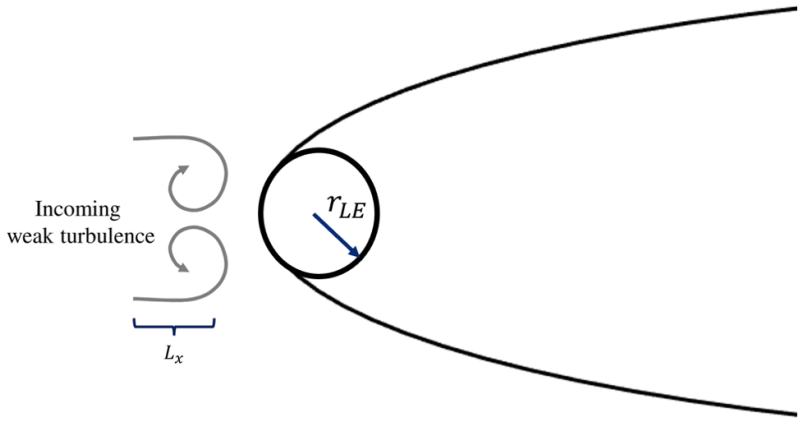

Figure 2.7: Representation of how Hunt's theory can be extended.

2.4 Propellers operating at low Reynolds numbers

A propeller is a propulsion machine consisting of rotating lifting surfaces disposed radially about a shaft that is aligned approximately with the direction of motion [34]. Due to its movement, the blade experiences various aspects of the fluid's relative velocity: the axial velocity resulting from the fluid's speed U_∞, the rotational velocity Ωr, and the induced velocity from the disruption caused by the propeller in the fluid. The two fundamental components of the resultant force to which the rotor is subjected are the thrust T and the torque Q. Trust and torque coefficients are defined as follows:

$$C_T = \frac{T}{\rho n^2 D^4} \qquad C_Q = \frac{Q}{\rho n^2 D^5} \tag{2.21}$$

where ρ is the air density, n the propeller rotational frequency and D the propeller diameter.
The propeller's operating conditions are commonly represented by three dimensionless groups: Mach number M, Reynolds number Re and advance ratio J.

$$M = \frac{U_\infty}{c_0} \qquad Re = \frac{\rho U_\infty L}{\mu} \qquad J = \frac{U_\infty}{nD} \tag{2.22}$$

This thesis seeks to investigate how a propeller behaves when operating at low Reynolds numbers. The Reynolds number significantly affects the performance of typical airfoils, notably causing a decline in aerodynamic efficiency for propellers when the Reynolds number falls below 10^5. An example of this can be seen in the figure 2.8, from Winslow *et al.*, where the trends of the lift, drag and pitching moment coefficients are shown for a NACA0012 profile as the Reynolds number varies. It is possible to notice that as the Reynolds number decreases the aerodynamic efficiency decreases. Additionally, the specific characteristics of an airfoil's boundary layer heavily influences its performance within distinct Reynolds number ranges [35].
The boundary layer on airfoils at low Reynolds numbers and moderate angles of attack is usually subjected to laminar separation; however, the separated shear layer quickly

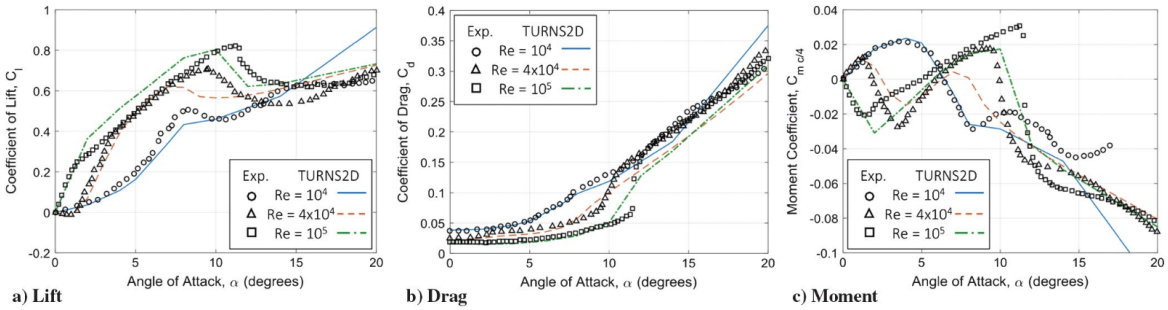

Figure 2.8: Lift, drag, and pitching moment comparison of CFD predictions for NACA0012 between Reynolds numbers of 10^4 and 10^5 (Experimental data from Ohtake *et al*) [35, 21].

undergoes turbulent transition and reattaches on the airfoil surface, forming a laminar separation bubble (LSB) [14].
The characteristics of this bubble, including its size and position, are influenced by the angle of attack, Reynolds number, and airfoil geometry. As the angle of attack (or Reynolds number) increases, the laminar separation bubble shifts closer to the leading edge and shrinks in length [14, 5]. Eventually, it bursts near the leading edge, resulting in a sudden reduction in lift and an increase in drag. In this scenario, a laminar separation occurs, but the free shear layer struggles to reattach immediately. This state is commonly referred to as a *long bubble*.
Grande *et al* [14] investigated the presence of the laminar separation bubble on the blade of a propeller rotating at 4000 rpm. Oil-flow visualization of the suction side of the propeller blade at b) J =0.24 (U_∞ =4.8 m/s), c) J =0.4 (U_∞ =8 m/s) and d) J =0.6 (U_∞ =12 m/s) are shown in figure 5.18. The thickness of the oil is larger in portions of the blade surface where the chordwise pressure gradient is almost zero, that is, in LSB and regions where the flow is simply separated, as at the root. The chordwise size of the LSB is determined from the distance between the laminar separation and reattachment lines, indicated in the figure with S and R, respectively.

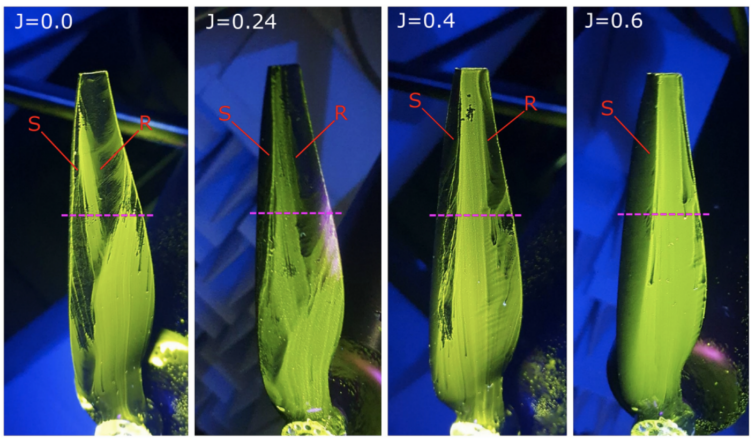

Figure 2.9: Oil-flow visualization of the suction side of the blade at 4000 rpm and J=0,0.24,0.4 and 0.6 [14].

The low-Reynolds number aerodynamic characteristics just illustrated are expected have also an influence on noise generation. This point will be addressed in more detail in the section 2.6.

2.5 Noise generated by propellers

Propellers produce two distinctly different types of noise: tonal or harmonic noise and broadband noise. The first one comes from sources that repeat themselves exactly during each revolution of the propeller, while the second one is a random non-periodic signal caused by turbulent flow over the blades [28, 13].

For an ideal propeller with B blades with shaft rotation and angular frequency Ω [rad/s], the fundamental component of the tonal noise will be at the blade passing frequency (BPF) $\Omega B/2\pi$ [Hz] and harmonics thereof.

On the other hand, propeller broadband noise is random in nature and contains components at all frequencies. It arises by the interaction of the blade with turbulence. Physically, turbulence gives rise to an upwash or downwash velocity and when it impinges on an airfoil or a blade the angle of attack undergoes a change due to the induced velocity related to the turbulence. This change in angle of attack causes a change in pressure distribution and thus load on the blade. Since turbulence is a random and continuous phenomenon, the variation in pressure distribution will be alike. This continuous variation on the pressure distribution is what we observe as noise. Specifically, noise generated by an unsteady phenomenon, such as turbulence, is defined as *unsteady loading noise* and is modeled by a dipole.

To establish the relative importance of tone and broadband noise we can consider noise spectrum of the signal. Figure 2.10 shows a typical noise spectrum for a conventional propeller [28].

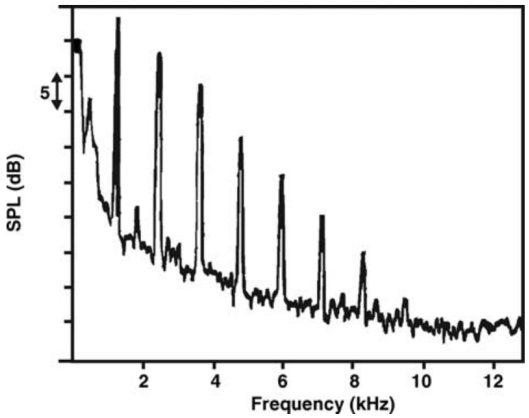

Figure 2.10: Conventional propeller noise spectrum, showing harmonics at blade passing frequency and broadband noise [28].

2.5.1 Blade-to-blade correlation and haystacking of broadband noise

A very important phenomenon to take into consideration when talking about inflow turbulence interacting with a propeller is haystacking that consists on the production of spectral humps at multiples of the blade passing frequency.
When the size of an eddy interacting with the blades is large enough to be cut multiple times by successive blades, then this lead to the loss of independence on how blades respond to the eddy itself. This correlation is called blade-to-blade coherence and it leads to a correlated unsteady loading on blades that are near one to another. From the point of view of the noise spectrum this phenomenon causes the appearance of peaks around the BPF and its harmonics.
The criterion for this effect to occur is that the BPF should be significantly higher than the axial inflow speed U_∞ divided by the axial turbulence length scale L_x, so that $\frac{B\Omega L_x}{U_\infty} \gg 1$. If this is a large parameter then blade-to-blade correlation needs to be considered [13].
So if we fix the number of blades B, the angular frequency Ω and the axial inflow speed U_∞ we can distinguish two cases:

- If L_x is small enough that the eddy is cut only once by one single blade we can avoid haystacking.
- Otherwise, if the propeller interacts with an eddy large enough to be cut by more than one blade consecutively then haystacking occurs.

In figure 2.11 , from [13], are shown the time history and the spectrum of the signal from interactions of rotor blades with a small eddy and a large eddy.

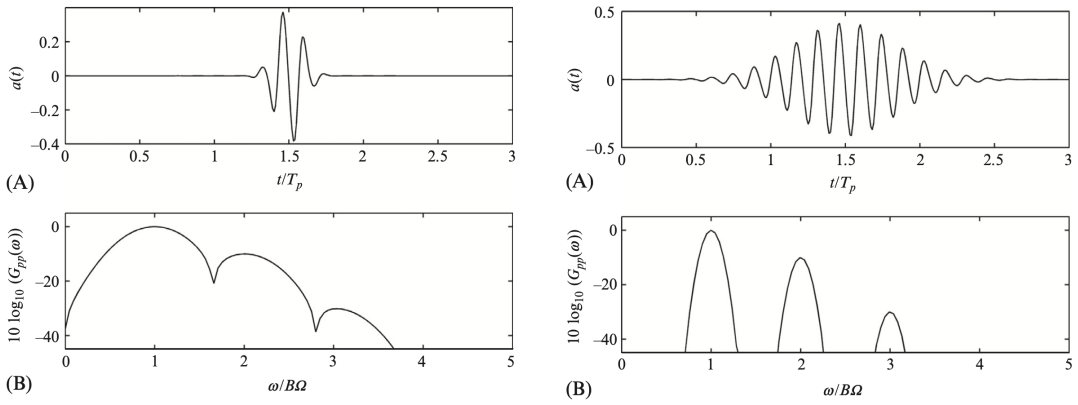

(a) Small eddy (b) Large eddy

Figure 2.11: Time history (A) and spectrum (B) from interactions of rotor blades with eddies of different size [13].

2.6 State of the art

As previously said, the noise radiated by a propeller is known to consist of a broadband, random signal on which are superimposed a number of discrete peaks. The peaks represent the tonal contribute of the noise and the sources of this type of noise are well understood since they were investigate for a long time.
Regarding broadband noise, we know that this is mainly due to random unsteady loads generated by turbulence in the inflow of the rotor.
The first one that investigated the effect of turbulence on unsteady loading noise of a propeller was Sevik [29]. He studied the sound radiated from a 10-baled open rotor subjected to homogeneous and isotropic turbulence created by means of two different type of grids, at subsonic speed. Figure 2.12 shows the comparison between theoretical prediction and experimental acoustic measurements. The "humps" in the measured spectrum occur at the blade passing frequency and Sevik assumed that they were caused by blade-to-blade coherence.

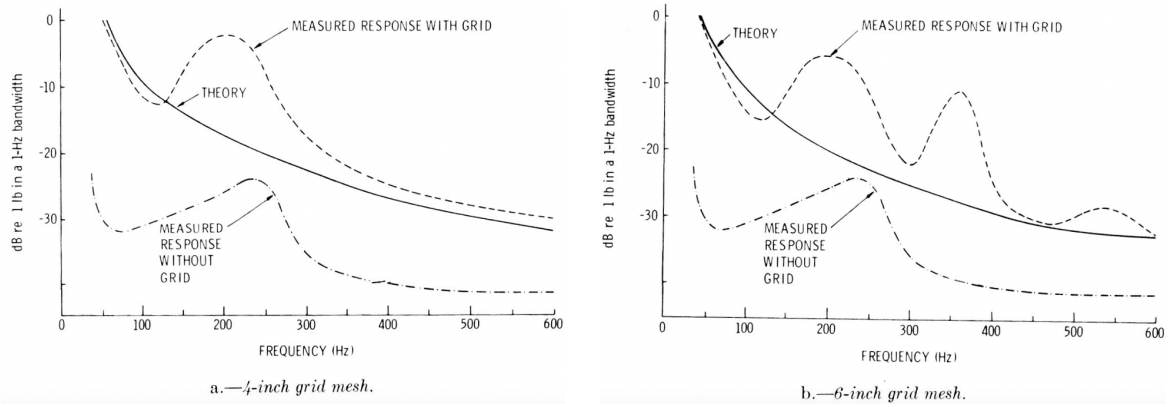

Figure 2.12: Comparison between theoretical prediction and experimental acoustic measurements by Sevik [29].

Hanson [15] examined how the characteristic of the static inlet turbulence can be related to the features of the narrow-band noise spectra caused by turbulence. Through his work he understood that eddies elongated due to contraction of the streamtube, caused by the presence of the rotor, interacted more frequently with the blades. This phenomenon leads to a coherence in the unsteady load of the blades, which in the noise spectrum is observed as peaks at the BPF and its harmonics.
Aravamudan and Harris [3] conducted experiments at the MIT anechoic wind tunnel to study the effects of controlled free-stream turbulence on the low-frequency broadband noise radiations from model rotor. Turbulence of varying intensity and scales was generated in the wind tunnel test section by means of biplanar grids of different sizes and then turbulence and acoustic data were analyzed. They discovered that low-frequency broadband noise intensity and spectra are dependent upon the rotor-tip velocity and the longitudinal integral length scale of turbulence. In particular, the peak intensity of the low-frequency broadband noise scales with M_{tip}^4 and with $(L_{uu}^z)^{-0.33}$.
Yauwenas *et al.* [36] investigated how disturbances in the incoming airflow affected the noise produced by a two-bladed drone propeller. The study encompassed experiments

conducted under two inflow conditions: a clean inflow and two distinct types of disturbances introduced upstream of the propeller. The first disturbance was induced by a mesh grid, while the second was caused by a wake created by a cylindrical object. Their findings (figure 2.13) demonstrated that the inflow disturbance caused by the cylinder wake amplified the overall noise level and introduced additional noise in the form of new harmonics at the beginning of the spectrum. Conversely, the grid-induced turbulence resulted in extra acoustic pulses at higher frequencies.

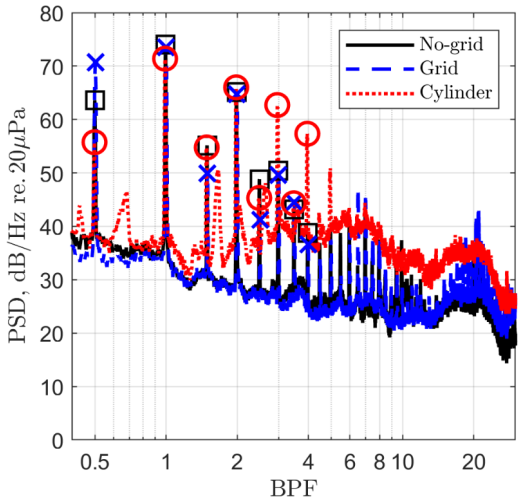

Figure 2.13: Acoustic pressure measurement for the three different cases analyzed by Yauwenas *et al.*

Talking about the effect of LSB contribution on noise, several studies on steady airfoils prove that the vortex shedding from an LSB can generate tonal or quasi-tonal noise. The effect of LSB on the noise produced by a propeller was investigated by Grande *et al* [14]. The far-field noise spectra at a fixed rpm of 4000 by varying the advance ratio J from 0 to 0.6 was studied and the results are shown in figure 2.14. In the hover condition, noise spectra display a more pronounced tonal component due to the fluctuating loads, in contrast to situations with positive advance ratios. The primary sources of broadband noise in the lower-to-middle frequency range vary depending on the advance ratio. In the case where J =0, turbulence-related noise resulting from airflow disturbances at the leading edge is considered the primary contributor. This turbulence is caused by the wake of the preceding blade. However, at J =0.24, 0,4 and 0.6 the trailing-edge noise source is expected to become the dominant one. On the other hand, the high frequency hump, visible for all the cases, is caused by the wake vortex shedding, originated from the laminar separation region.

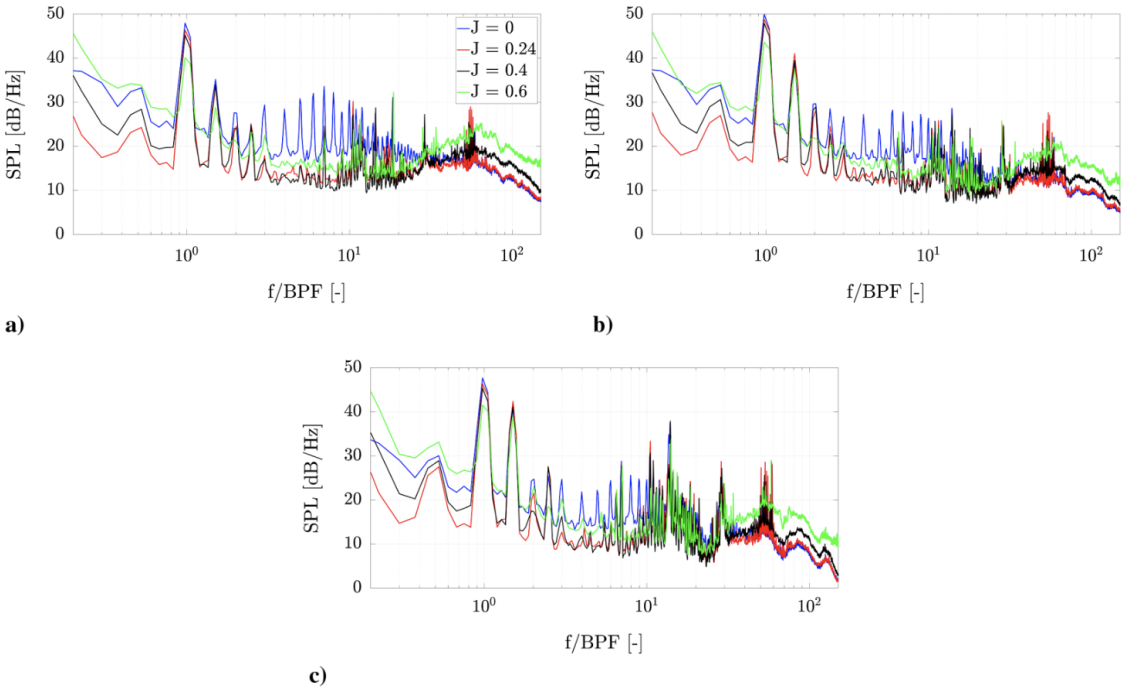

Figure 2.14: Comparison of noise spectra at 4000 rpm measured with a) mic 3, b) mic 7, and c) mic 11 by varying the advance ratio J from 0 to 0.6 [14].

2.6.1 Noise prediction models

Peterson and Amiet [22] proposed a theoretical and experimental investigation of the noise of a model helicopter rotor due to the ingestion of grid-generated, isotropic turbulence. Far field noise spectra and directivity were measured in addition to inflow turbulence intensities, length scales and spectra. Then, measured inflow turbulence statistics and rotor operating parameters were employed in a theoretical procedure to predict turbulence ingestion noise spectra and directivity. From this study they concluded that incident turbulence represents a potentially important source of rotor narrowband random (quasi-tonal) and broadband noise. The prediction method showed good agreement between theory and experiment, especially for high frequency broadband noise and if it is considered a thin airfoil. Hence, in cases where reasonable estimates of incident turbulence statistics can be made, the theory provides a means to predict the contribution of turbulence ingestion noise to overall rotor noise spectra and directivity.
The principal problem of this model is that it doesn't take into account the alteration of the velocity field (i.e. the turbulence distortion) caused by the contraction of the streamtube and by the real geometry of the blades. Indeed, the theory models turbulence using a canonical turbulence spectrum, such as the Von Karman ones, hence neglecting the distortion to which the turbulence is subjected near the leading edge.
The effects of turbulence distortion on noise generation and the role of aerofoil geometry were widely investigated by Chaitanya *et al.* [6], who concluded that the aerofoil thickness and leading-edge shape are the main geometrical characteristics affecting the noise-generation efficiency, with the latter being particularly relevant in the high-

frequency range.
Considering the rapid distortion theory by Hunt and its extension to the case of the airfoil leading edge, Moreau and Rogers [19] proposed a modification of the analytical expression of the canonical turbulence spectrum used as input into Amiet's model to account for the distortion of small-scale structures caused by the presence of the body: a correction of the slope of the von Karman spectrum in the high-frequency range from $-5/3$ to $-10/3$, based on the findings of the RDT, was introduced. Some results of their study can be seen in figure 2.15. A satisfactory correspondence was established between experimental measurements and the high-frequency decay rate of the far-field noise spectrum and noise levels.

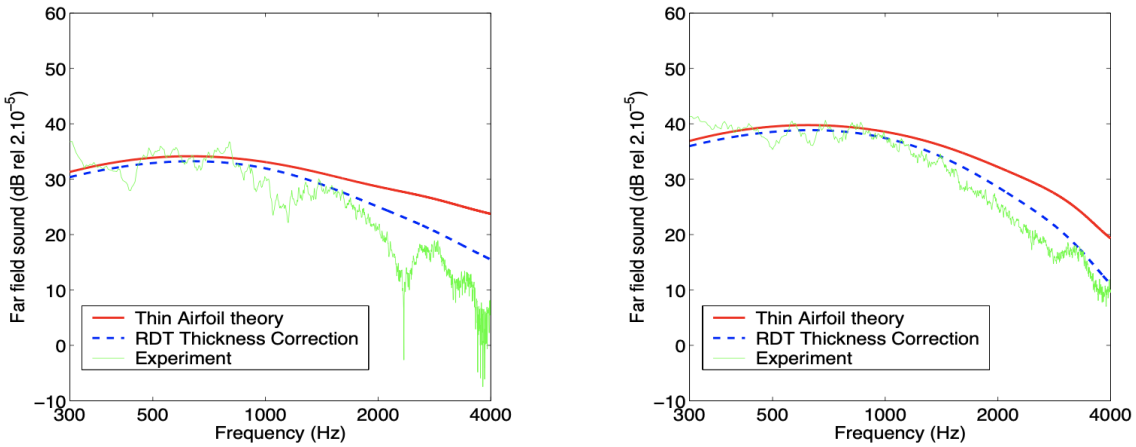

Figure 2.15: Comparison between all models and experimental spectra for the NACA0012 airfoil at 30° (left) and 70° (right), conducted by Moreau and Rogers.

However, it's important to note, as pointed out by the authors, that the accuracy of the adjustment was confined to the specific scenario under examination and would be challenging to apply universally if the features of the distorted turbulence were not adequately modeled.
A similar approach was followed by dos Santos *et al* [26] who proposed an empirical correction to better predict turbulence spectra in the dissipation range through a modified von Karman expression. The corrected turbulence spectrum was then used as input in Amiet's model to improve the prediction accuracy in the high-frequency range. However, the method's effectiveness in predicting leading-edge noise relies on singling out a representative location within the flow field. This specific point should be representative of the flow dynamics, allowing for the sampling of integral length scale and turbulence intensity: crucial parameters necessary to calibrate the suitably refined analytical von Karman expression.

3

Analytical noise-prediction model

This chapter introduces the analytical model employed to predict the far-field acoustic power pressure density generated by a propeller subjected to turbulent flow. The model leads to the prediction of the Power Spectral Density (PSD) by leveraging key turbulence parameters. The final model for the rotor noise prediction has been obtained starting with a formulation valid for the case of an airfoil in rectilinear motion.

3.1 Acoustic predictive model for an airfoil

With reference to [2], an airfoil of chord $2b$ and span $2d$, placed in a turbulent flow with a mean free-stream velocity U in the x-direction has been considered. The origin of the coordinate system is at the center of the airfoil and the y-direction is along the span. If we consider a gust of the form:

$$w_g = w_0 e^{i[k_x(x-Ut)+k_y y]} \tag{3.1}$$

the distribution of the airfoil pressure jump modelled as a flat plate of infinite span can be written as:

$$\Delta P(x, y, t) = 2\pi\rho_0 U b w_0 g(x, k_x, k_y) e^{i(k_y y - k_x U t)}\, dk_x\, dk_y \tag{3.2}$$

where $g(x, k_x, k_y)$ is the transfer function between turbulent velocity and airfoil pressure jump. Integrating now over all the wavenumber components and applying the Fourier transform with respect to time, it is possible to obtain the total pressure jump in the frequency domain:

$$\Delta P_T(x, y, \omega) = 2\pi\rho_0 b \int_{-\infty}^{\infty} w_R(K_x, k_y) g(x, K_x, k_y) e^{ik_y y}\, dk_y \tag{3.3}$$

where $K_x = -\omega/U$. Now it is possible to introduce the the cross-PSD, S_{QQ}, of the pressure jump between two points on the surface. The cross-PSD can be written as:

$$S_{QQ}(x_1, x_2, y_1, y_2, \omega) = \lim_{T\to\infty} \left\{ \frac{\pi}{T} E\big[\Delta P_T^*(x_1, y_1, \omega) \Delta P_T(x_2, y_2, \omega)\big] \right\} \tag{3.4}$$

where $E[\dots]$ is the expected value or ensemble average of a quantity. Considering equation 3.3, w_R is the only non-deterministic quantity, so if we have to substitute

equation 3.3 into equation 3.4, all terms except w_R can be taken outside $E[\dots]$, leaving $E\big[w_R(K_x,k_y)w_R^*(K_x,k_y')\big]$. Due to the statistical orthogonality of the wavevectors, it can be demonstrated that:

$$E\big[w_R(K_x,k_y)w_R^*(K_x,k_y')\big] = \frac{R}{\pi}\delta(k_y-k_y')\phi_{ww}(K_x,k_y') \tag{3.5}$$

where ϕ_{ww} is the turbulence spectrum. Combining equations 3.3 and 3.5 we obtain the following expression:

$$S_{QQ}(x_1,x_2,\eta,\omega) = (2\pi\rho_0 b)^2 U\int_{-\infty}^{\infty} g^*(x_1,K_x,k_y)g(x_2,K_x,k_y)\phi_{ww}(K_x,k_y)e^{ik_y\eta}\,dk_y \tag{3.6}$$

where $\eta = y_2 - y_1$ is the spanwise separation of the two points on the airfoil surface between which the PSD is performed.
Kirchhof and Curle's theories state that the acoustic response of an airfoil can be determined by a distribution of dipoles on the surface of the airfoil equal in intensity to the force exerted on the surface. Applying these theories it is possible to relate the cross-PSD of the surface pressure to the far-field noise. For example, the far-field sound produced by a point force of strength $F(x_0,y_0,\omega)e^{i\omega t}\mathbf{k}$ in a stream of Mach number M is:

$$P(x,y,z,\omega;x_0,y_0) = \frac{i\omega F(x_0,y_0,\omega)}{4\pi c_0\sigma^2}e^{i\omega\left[t+\frac{M(x-x_0)-\sigma}{c_0\beta^2}+\frac{xx_0+yy_0\beta^2}{c_0\beta^2\sigma}\right]} \tag{3.7}$$

where $\sigma = \sqrt{x^2+\beta^2(y^2+z^2)}$ and $\beta = \sqrt{1-M^2}$. In our case the force is equal to the pressure jump and the far-field pressure can be found integrating equation 3.4 over the airfoil planform area. This integration result is then multiplied by its complex conjugate, and upon taking the expected value, it establishes a connection between the power spectral density (PSD) of the far-field noise, denoted as S_{PP}, and the cross-PSD of airfoil loading:

$$S_{PP}(x,y,z,\omega) = \Big(\frac{\omega z}{4\pi c_0\sigma^2}\Big)^2\iiiint S_{QQ}(x_1,x_2,\eta,\omega) \\ e^{\frac{i\omega}{c_0}[\beta^2(x_1-x_2)(M-x/\sigma)+y\eta/\sigma]}\,dx_1\,dx_2\,dy_1\,dy_2 \tag{3.8}$$

By substituting the expression 3.4 into the equation 3.8, we obtain an expression for the far-field PSD as a function of the turbulence energy spectrum and the airfoil response function:

$$S_{PP}(x,y,z,\omega) = \Big(\frac{\omega z\rho_0 b}{c_0\sigma^2}\Big)^2 U\pi d\int_{-\infty}^{\infty}\Big[\frac{\sin^2\left(d(k_y+\omega y/c_0\sigma)\right)}{(k_y+\omega y/c_0\sigma)^2\pi d}\Big] \\ |\mathscr{L}(x,K_x,k_y)|^2\phi_{ww}(K_x,k_y)\,dk_y \tag{3.9}$$

where $\mathscr{L}(x,K_x,k_y)$ is the chordwise integral of the surface loading.

$$\mathscr{L}(x,K_x,k_y) = \int_{-b}^{b} g(x_0,K_x,k_y)e^{-i\omega x_0(M-x/\sigma)/c_0\beta^2}\,dx_0 \tag{3.10}$$

This function, also known as the aeroacoustic transfer function, is able to predict the aerodynamic and the aeroacoustic response of the airfoil to the gust. The implementation of this function follows the expression given by de Santana et al. [11, 10], as shown

below. $\mathscr{L}$ is obtained by adding two contributions: $\mathscr{L}_1$, representing the leading-edge term, and $\mathscr{L}_2$, representing the trailing-edge term.

$$\mathscr{L}_1(x,y,z,k_x,k_y) = \frac{1}{\pi}\sqrt{\frac{2}{(\bar{k}_x+\beta^2\kappa)\theta_1}}E^*(2\theta_1)e^{i\theta_2} \tag{3.11}$$

$$\mathscr{L}_2(x,y,z,k_x,k_y) \simeq \frac{e^{i\theta_2}}{\pi\theta_1\sqrt{2\pi(\bar{k}_x+\beta^2\kappa)}} \left\{ i\big(1-e^{-2i\theta_1}\big) + (1-i)\Big[E^*(4\kappa) - \sqrt{\frac{2\kappa}{\theta_3}}e^{-2i\theta_1}E^*(2\theta_3)\Big]\right\} \tag{3.12}$$

where $\theta_1 = \kappa - \mu x/\sigma_0$, $\theta_2 = \mu(M - x/\sigma_0) - \pi/4$, $\theta_3 = \kappa + \mu x/\sigma_0$, $\kappa^2 = \mu^2 - \bar{k}_z/\beta^2$ and $\mu = \bar{k}_x M/\beta^2$. The symbol $(\bar{.})$ represents the normalization of the wavenumbers obtained by multiplying them by half the chord $c/2$. The function $E^*(x)$ is a combination of the Fresnel's integrals C_2 and S_2 with the following expression:

$$E^*(x) = \int_0^x \frac{e^{-it}}{\sqrt{2\pi t}}\,dt = C_2(x) - iS_2(x) \tag{3.13}$$

with

$$C_2(x) = \frac{1}{\sqrt{2\pi}}\int_0^x \frac{\cos t}{\sqrt{t}}\,dt \tag{3.14}$$

$$S_2(x) = \frac{1}{\sqrt{2\pi}}\int_0^x \frac{\sin t}{\sqrt{t}}\,dt \tag{3.15}$$

Finally we have that:

$$\mathscr{L} = \mathscr{L}_1 + \mathscr{L}_2 \tag{3.16}$$

The primary assumption up to this point, aside from employing the linearized airfoil theory, has been to consider the infinite-span airfoil hypothesis. Amiet showed that considering $d \to \infty$ it is possible to write:

$$S_{PP}(x,y,z,\omega) = \Big(\frac{\omega z \rho_0 b}{c_0\sigma^2}\Big)^2 \pi U d \left|\mathscr{L}\Big(x, K_x, \frac{\omega y}{c_0\sigma}\Big)\right|^2 \phi_{ww}\Big(K_x, \frac{\omega y}{c_0\sigma}\Big) \tag{3.17}$$

Now consider the simplified case of an observer in the y=0 plane, i.e the case of a listener in the midspan plane of the airfoil. The equation just written becomes:

$$S_{PP}(x,0,z,\omega) = \Big(\frac{\omega z \rho_0 b}{c_0\sigma^2}\Big)^2 \pi U d \big|\mathscr{L}(x,K_x,0)\big|^2 \phi_{ww}(K_x,0) \tag{3.18}$$

Under the assumptions presented above it is possible to rewrite in a different way the two-dimensional wavenumber spectrum by introducing the cross-correlation length, $l_y(\omega)$, as a function of frequency. When we perform the Fourier transform of $\phi_{ww}(K_x,k_y)$

with respect to k_y, the resulting function $R_{ww}(K_x, y)$, represents U times the cross-power spectral density (PSD) of vertical velocity fluctuation between two points separated by a distance y. Integrating this function over y is expected to yield a value proportional to a correlation length. In practice, a correlation length, $l_y(\omega)$, can be defined based on this integration.

$$l_y(\omega) = \frac{1}{R_{ww}(K_x, 0)} \int_0^\infty R_{ww}(K_x, y)\, dy = \pi \frac{\phi_{ww}(K_x, 0)}{R_{ww}(K_x, 0)} \tag{3.19}$$

Then, equation 3.18 can be rewritten as:

$$S_{PP}(x, 0, z, \omega) = \left(\frac{\omega z \rho_0 b M}{\sigma^2}\right)^2 d \left|\mathscr{L}(x, K_x, 0)\right|^2 l_y(\omega) S_{ww}(\omega) \tag{3.20}$$

where $S_{ww}(\omega) = R_{ww}(K_x, 0)/U$ is the PSD of the vertical velocity fluctuations.
To model $l_y(\omega)$ and $S_{ww}(\omega)$ the incoming turbulence has been considered isotropic. The expression for the spanwise coherence length has been taken from Amiet [2] and is the following:

$$l_y(\omega) = \frac{8 L_{uu}}{3} \left[\frac{\Gamma(1/3)}{\Gamma(5/6)}\right]^2 \frac{\hat{K_x}^2}{\left(3 + 8\hat{K_x}^2\right)\sqrt{1 + \hat{K_x}^2}} \tag{3.21}$$

where $\hat{K_x} = K_x/k_e$ and

$$k_e = \frac{\sqrt{\pi}}{L} \frac{\Gamma(5/6)}{\Gamma(1/3)}. \tag{3.22}$$

To model $S_{ww} = R_{ww}/U$, the expression for R_{ww} has been taken from Glegg [13], in particular:

$$R_{ww}(K_x) = \frac{2}{27\sqrt{\pi}} \frac{\Gamma(5/6)\overline{u'^2}}{\Gamma(7/3) k_e} \frac{3 + 8(K_x/k_e)^2}{\left[1 + (K_x/k_e)^2\right]^{11/6}} \tag{3.23}$$

Equations 3.17 through 3.20 represent the final result obtained by Amiet to predict the sound produced by an airfoil in a turbulent flow.

3.2 Predictive model extended to a rotor

The theory presented above can be applied to a rotor scenario with a few adjustments, as demonstrated by Amiet in his 1989 paper. The key procedures are outlined in the following sections, for the complete analysis refer to [1].

3.2.1 Airfoil in circular motion

Under certain conditions and assumptions, the previous result obtained for an airfoil in straight-line motion can be extended to analyze the noise generated by a rotor. Firstly, geometrical relations concerning the moving position of the blade with respect to the listener must be identified. The illustration of the geometry of the problem is depicted in figure 3.1. The origin of the (x, y, z) coordinate system is fixed to the rotor hub. The x and y axes lie on the rotor plane, while the z-axis is along the rotor axis, with

the axial component of flow velocity being negative in the z-direction. The observer is fixed in the x-z plane at a distance r from the rotor hub, making an angle θ between the z-axis and the line from the hub and the observer itself. The position of the observer with respect to the rotor hub is:

$$\mathbf{x}_0 = r(\sin\theta\hat{i} + \cos\theta\hat{k}) \tag{3.24}$$

$\mathbf{M}_f$ represents the non-axial component of the flow an it is placed at an angle ψ to the y-axis. The angle γ is the angle that the blade span makes with the x-axis, i.e $\gamma = \omega t$. So we can define the following Mach numbers:

$$\mathbf{M}_z = -M_z\hat{k} \tag{3.25}$$

$$\mathbf{M}_f = -M_f(\sin\psi\hat{i} + \cos\psi\hat{j}) \tag{3.26}$$

$$\mathbf{M}_s \equiv \mathbf{M}_f + \mathbf{M}_z \qquad\qquad M_s^2 = M_f^2 + M_z^2 \tag{3.27}$$

Moreover, since the blade is considered a flat plate with zero steady loading, we can define with α the angle that a blade segment makes with the x-y plane as:

$$\cot\alpha = \frac{M_t + M_f\cos(\gamma + \psi)}{M_z} \tag{3.28}$$

where M_t is the azimuthal Mach number of the blade segment relative to the rotor hub. The equation 3.20 that describes the far-field behavior of an airfoil in linear motion

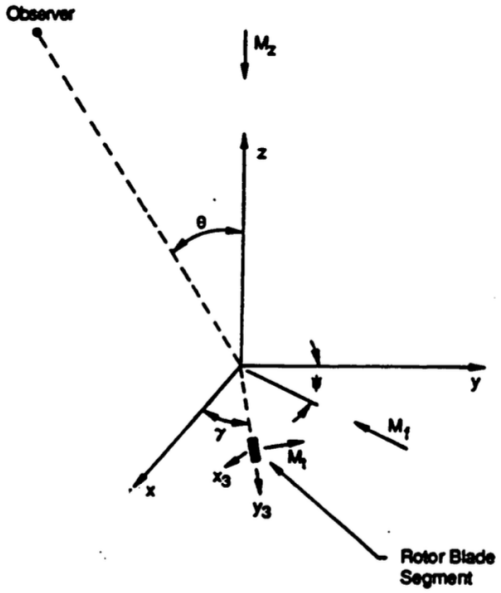

Figure 3.1: Geometry of rotor problem, from [1].

is formulated based on the current airfoil position. To extend this relationship to a rotating airfoil segment, it is essential to calculate the equivalent of the present position

for that specific segment. The term "present position" refers to the location of the airfoil segment with respect to the fluid, assuming it follows a straight path during the time it takes for the sound to travel from the source to the observer. Therefore, it is crucial to determine the observer's position with respect to the sound source. Consequently, the retarded source position of the airfoil segment needs to be considered. This can be understood by considering the example of the sound produced by a marker in the fluid. When a marker is placed in the fluid and a sound is generated at the beginning time $t = 0$, as the sound reaches the observer, a certain amount of time $t = T_e$ passes,while the marker has moved to a different position identified as $\mathbf{x}_s$. The observer is at $\mathbf{x}_0$ and the distance r_e of the observer from the retarded source point is:

$$r_e^2 = (r\sin\theta - x_s)^2 + y_s^2 + (r\cos\theta - z_s)^2 \tag{3.29}$$

Also $T_e = r_e/c_0$ and than considering the equations 3.25 and 3.26, the retarded coordinates are:

$$\begin{cases} x_s = -T_e c_0 M_f \sin\psi = -M_f r_e \sin\psi \\ y_s = -M_f r_e \cos\psi \\ z_s = -M_z r_e \end{cases} \tag{3.30}$$

Substituting equations 3.30 into equation 3.29 we can write:

$$r_e = \frac{r\left(M_s\cos\Theta + \sqrt{1 - M_s^2\sin^2\Theta}\right)}{1 - M_s^2} \tag{3.31}$$

where Θ is the angle between the convection Mach number, $\mathbf{M}_s$, and the vector linking the observer and the source.
The current source position $\mathbf{x}_p$ can be obtained by adding to $\mathbf{x}_s$ the chordwise displacement of the airfoil during the specified time interval ($t = T_e$):

$$\mathbf{x}_p = \mathbf{x}_s + \mathbf{M}_b c_0 T_e \tag{3.32}$$

where $\mathbf{M}_b$ is the chordwise component of the rotor segment Mach number:

$$\mathbf{M}_b = [M_t + M_f\cos(\gamma + \psi)](-\sin\gamma\hat{i} + \cos\gamma\hat{j}) + M_z\hat{k}. \tag{3.33}$$

So, for a coordinate system at this present source position the observer has coordinate $\mathbf{x}_1$ given by:

$$\mathbf{x}_1 = \mathbf{x}_0 + \mathbf{x}_p \tag{3.34}$$

Equation 3.20 is applicable to a coordinate system in which the airfoil lies in the x-y plane, with the span along the y-direction. For this reason the coordinate system above ($\mathbf{x}_1$) has to be rotated about the z-axis by an angle $\pi - \gamma$ in order to have the same orientation with respect to the airfoil. This yields a new system, called $\mathbf{x}_2$ system, with y_2 aligned with the airfoil span. Then, rotating this new system about the y_2-axis by an angle α we obtain the $\mathbf{x}_3$ system, with x_3 along the chord, pointing from leading to trailing edge. The observer coordinates in the $\mathbf{x}_3$ system are the ones required in equation 3.20, and they can be written as follows:

$$\begin{cases} x_3 = r_e M_t\cos\alpha - r_0\cos\Phi \\ y_3 = x_0\cos\gamma + M_f r_e\sin(\gamma + \psi) \\ z_3 = (x_0\sin\gamma + r_e M_t)\sin\alpha + z_0\cos\alpha \end{cases} \tag{3.35}$$

where $r_0^2 = x_0^2 + y_0^2 + z_0^2$ and $\cos\Phi = \cos\theta\cos\alpha - \sin\theta\sin\gamma\cos\alpha$.

3.2.2 Inverse strip theory

The model introduced by Amiet considers an aifoil whose geometrical characteristics do not vary in the spanwise direction, which is not true in the case of propellers. Consequently, dealing with spanwise-varying inflow conditions poses a significant challenge in noise calculation in the case of rotors and fans. In this work, the problem is addressed by employing inverse strip theory, starting from the results of the work conducted by Miotto et al [17]. To take into account spanwise-varying flow conditions along the airfoil, a possible approach involves discretizing the airfoil into individual strips, each characterized by its distinctive impacting flow conditions. The total noise produced by the complete airfoil corresponds to the sum of contributions from each individual strip. When the airfoil is divided into discrete strips, it is important to recognize that the assumption of infinite span, as commonly employed in equation 3.20, may not hold true for each specific strip. For this reason the more general formulation, provided by equation 3.9 should be used. Christophe et al. [8] discovered that the direct strip approach was inaccurate in the low-frequency regime, so they proposed the inverse strip theory to overcome the theoretical limitation of the direct strip approach. The proposed solution was to generate small span strips with a combination of large span airfoils, as illustrated in figure 3.2(a). This method allows the use of formulation 3.20 which allows to accurately replicate the radiated noise across the entire frequency spectrum and it is computationally less expensive compared to formulation 3.9.
In the inverse strip approach, the noise generated by an airfoil strip is calculated from the subtraction of the sound computed for two extensive-span airfoils. These airfoils have span lengths that vary by the length of the small strip segment currently being examined. Figure 3.2(b) provides a visual depiction of the operational principles of the inverse strip method. In this graphical representation, the involvement of each strip, denoted by $n = 1, \ldots, N$, is determined through the contrast between the pressure Power Spectral Density (PSD) of a large-aspect-ratio (virtual) wing using the infinite-span formulation (depicted as S_{PP}^{∞}) and another (virtual) wing positioned at the same location. However, the span length of this second wing is diminished by the size δ of the strip, as illustrated by $S_{PP}^{(\infty-n)}$. This visual aid illustrates the process wherein the noise contribution from each strip is calculated. So the resulting PSD is:

$$S_{PP} = \sum_{n=1}^{N} \left(S_{PP}^{\infty} - S_{PP}^{(\infty-n)} \right) \tag{3.36}$$

where both S_{PP}^{∞} and $S_{PP}^{(\infty-n)}$ are calculated through equation 3.20.

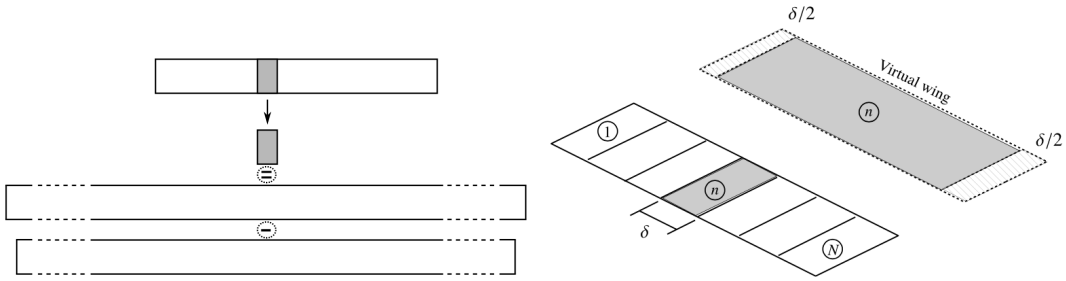

Figure 3.2: Representation of the inverse strip method based on a combination of large span airfoils, from [17, 8]

3.2.3 Doppler effect

Equations 3.35 provide the suitable instantaneous observer coordinates for calculating the sound spectrum from equation 3.20. It is important to notice that the angle $\gamma = \omega t$ is a time-dependent function. To compute the time-averaged spectrum, an average around the azimuth must be determined. This average needs to consider both the Doppler shift in frequency as the airfoil segment moves relative to the observer and the delayed time effects as the blade rotates around the azimuth. The latter correction is necessary because the blades spend varying amounts of time, in the acoustic sense, at each azimuthal position. The appropriate azimuthal weighting is given by the Doppler factor:

$$\frac{\omega}{\omega_0} = 1 + \frac{M_t[x_3 \sin\gamma - M_f r_e \cos(\gamma + \psi)]}{\sqrt{1 - (M_f^2 + M_z^2)\sin^2\Theta}} \tag{3.37}$$

where ω is the frequency of the airfoil forces and ω_0 is the Doppler-shifted frequency. The azimuthally averaged spectrum is then:

$$S_{PP}(\mathbf{x}, \omega) = \frac{1}{2\pi} \int_0^{2\pi} \frac{\omega}{\omega_0} S_{PP}(\mathbf{x}, \omega_0, \gamma)\, d\gamma \tag{3.38}$$

4

Experimental set-up

This chapter presents the experimental set-up and describes the conditions under which the experiments were carried out.

4.1 Wind tunnel set-up, flow conditions and propeller design

The experiments were carried out in the anechoic tunnel (A-tunnel) at the low-speed laboratory of TU Delft. The A-tunnel is an open-jet, closed-circuit, vertical wind-tunnel, where the surrounding of the nozzle exit consists of an anechoic chamber with the walls covered by melamine wedges. The nozzle exit has a diameter of 0.6 m and the free-stream velocity was set to 9 m/s.
The design of the A-tunnel allows for the use of interchangeable nozzles that can be flush-mounted to the exit of the contraction. A grid was placed at the contraction's exit to generate a desired level of turbulence intensity. The contraction then terminated with a cylindrical nozzle with constant section.
The grid has a mesh size G of 100 mm, the width of the rods d is of 10 mm and their thickness t is 5 mm. The distance between the grid and the propeller is equal to 10 mesh size, i.e. 1 m.
The rotor used in this research is the same one used by Grande *et al* [14] in their study. The propeller design derives from an APC 9×6 model aircraft two-bladed propeller, which typically functions at a low Reynolds number, featuring a 9″ (22.86 cm) diameter and a 6″ (15.24 cm) pitch. The diameter has been scaled up to D =30 cm and each profile has been reshaped with an NACA4412 airfoil. Additionally, an elliptical section at the root has been merged with the first profile section starting from a radius of 1 cm. The maximum chord is c_{max} =2.4 cm and the maximum twist angle is β_{max} = 43.6°. The propeller, made of aluminum alloys, was manufactured through computer numerical control machining at TU Delft, achieving a surface finish with roughness values in the range of 0.4 to 0.8 µm Ra. This machining process ensures precision and reduces surface flaws, which could otherwise lead to vibrations during measurements and impact the flow quality around the propeller blades.
The rotational plane of the propeller is aligned with the grid, resulting in a 90° angle between the propeller plane and the direction of the flow.

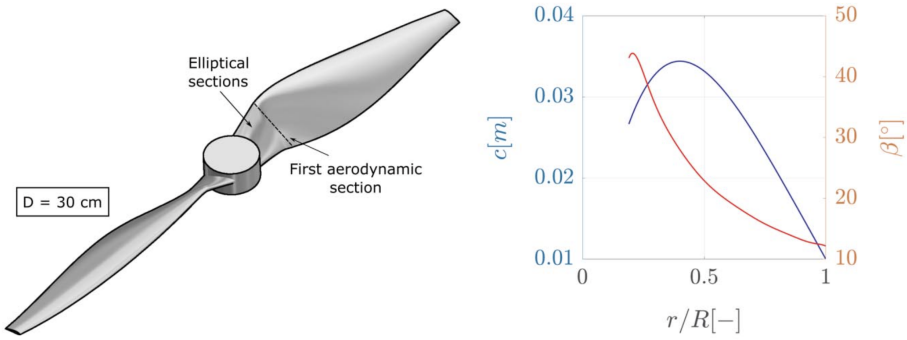

Figure 4.1: Propeller CAD geometry and blade chord and pitch angle distributions [14].

4.1.1 Propeller test rig

The propeller is attached to a streamlined aluminum housing with a 5 cm diameter to reduce its impact on the propeller's airflow. Inside this housing, there are various components, including a motor, an encoder, a load cell, and a torque cell. The housing is supported by reinforced hollow aluminum profiles with a NACA0012 shape and a 6 cm chord. These profiles also contain the necessary cables, which are connected remotely to the equipment located outside the tunnel. To keep the entire structure stable and minimize vibrations and interference, it is suspended above the tunnel's nozzle using four steel-wire tubes with a 2 cm diameter. These tubes are securely fixed to the tunnel. The propeller is driven by a brushless electric motor, AXI 2835/10 Gold Line V2 Long whose technical characteristics are shown in table 4.1. The motor is powered by a Delta Elektronika DC power supply with a voltage range of 0-15 V and a current range of 0–100 A. The rotational speed of the motor is determined using a US Digital EM1 transmissive optical encoder. This encoder is connected to a US Digital disk with a diameter of 25.4 mm, and the disk generates 200 cycles for every complete revolution.

Name	AXI 2835/10 Gold Line V2 Long
RPM/V	690
Max efficiency current	12-26 A
No load current	2.8 A
Currenty capacity	69A/60s
Dimensions ($\varnothing$xL)	35x75.5 mm
Max power	1190 W

Table 4.1: Technical specifications of the motor.

The engine is connected to an ATI-Mini40 torque/load cell that measures in the vertical (x) direction, with a capacity of up to 60 N and an accuracy of 0.75%. Additionally, it measures forces in the z and y directions, with capacities of up to 20N and accuracies of 1% and 1.25%, respectively. The resolution is 1/100 N for the x-direction and 1/200N for the z and y directions. Torque measurements are accurate up to 1 Nm in all three

directions, with a resolution of 1/8000 Nm.

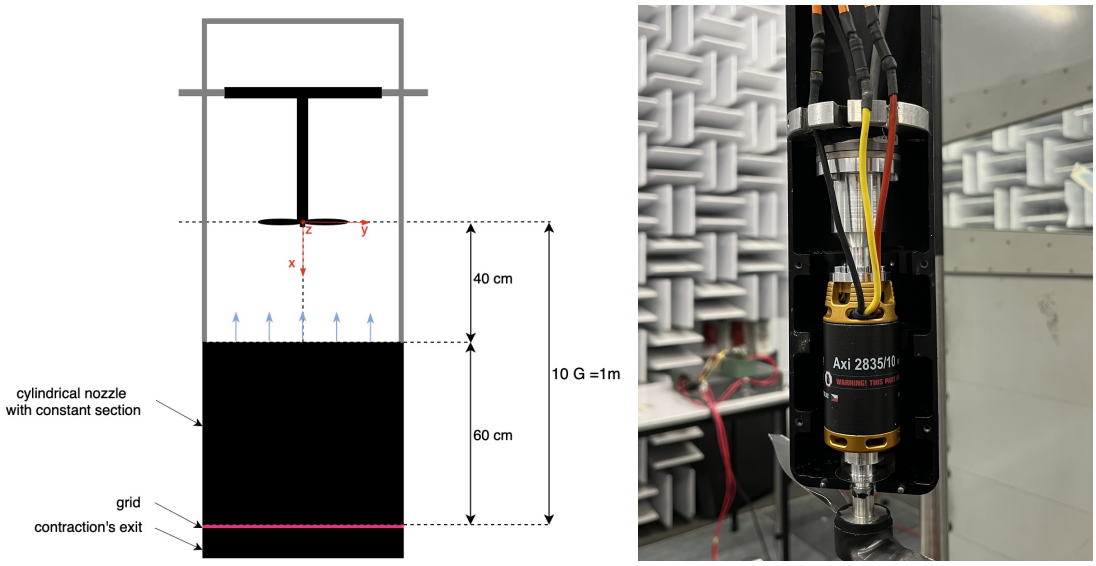

(a) (b)

Figure 4.2: Propeller set-up (a) and propeller drive train (b).

4.2 HWA measurements

Hot wire anemometry measurements were conducted to evaluate the characteristics of the flow field downstream the grid, near the propeller plane. Measurements were made both in the presence of the rotor and in its absence to investigate how the presence of the propeller changes the turbulent flow field.
A probe manufactured by Dantec Dynamics (probe type 55P11) whose technical specifications are listed in table 4.2 was used for the acquisitions. The probe is driven by a constant temperature bridge and the hot wire is positioned to measure the velocity in the direction of the fluid flow.
The probe was mounted on a remotely controlled 2D traversing system, as shown in figure 4.3. The hot wire is positioned to measure the velocity in the streamwise direction. Measurements are performed at a sampling frequency of 51.2 kHz for a duration of 60 s. Figure 4.4 shows the hot wire measurement locations in the flow field.

Name	Dantec Dynamics type 55P11
R_{20}	$3.15\,\Omega$
R_L	$0.5\,\Omega$
α_{20}	$0.36\,\%/°C$

Table 4.2: Technical specifications of the hot wire probe.

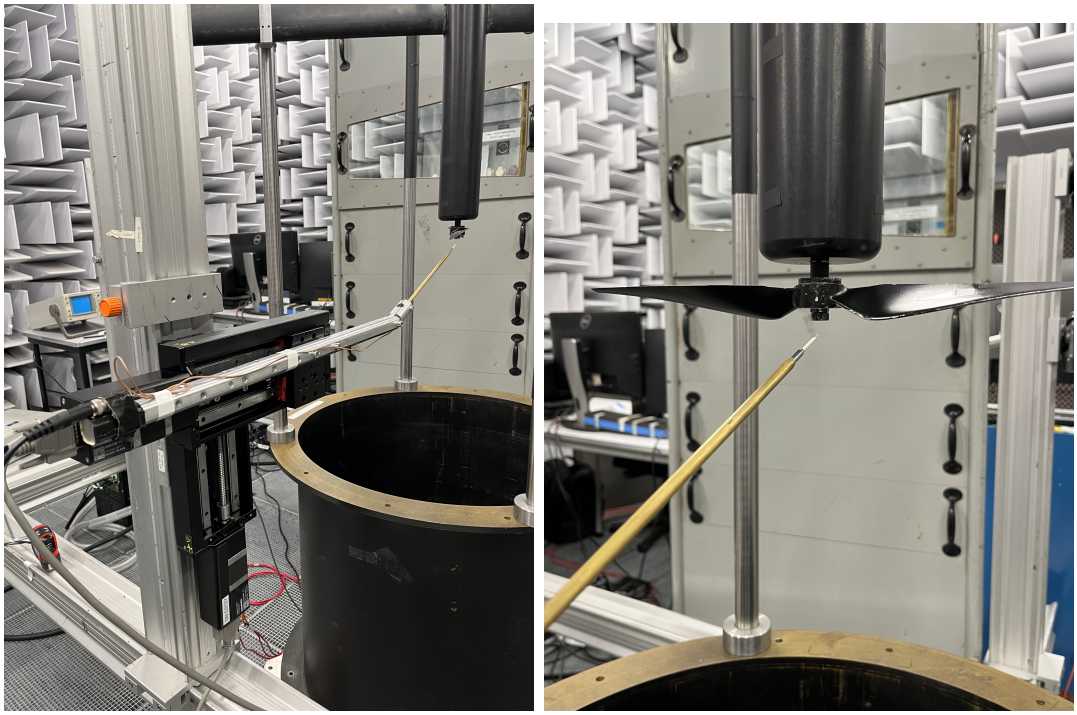

(a) (b)

Figure 4.3: Hot wire set-up: (a) 2D traversing system, hot wire probe and probe holder mounted in the A-Tunnel, (b) orientation of the probe.

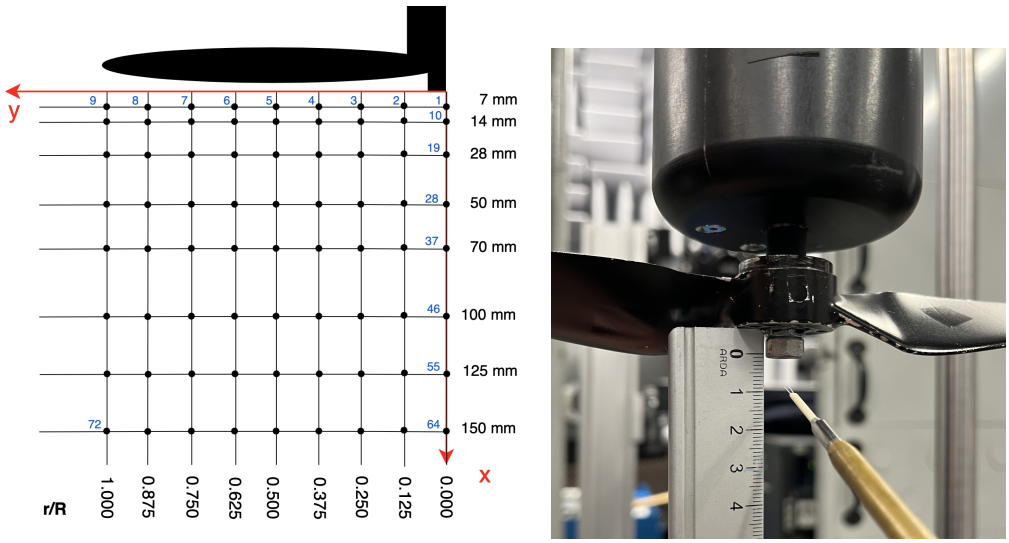

(a) (b)

Figure 4.4: Hot wire measurement locations denoted with black dots (a) and closest point to the rotor (b).

4.3 Acoustic measurements

For the acoustic measurements, a microphone arc containing 7 G.R.A.S. 40 pH free-field microphones has been used. Each microphone has a diameter of 7 mm, a frequency range between 10 and 20 kHz, and a maximum sound pressure level (SPL) of 135 dB . The reference pressure is 20 µPa and the microphones have an integrated CCP preamplifier.
The microphones can be mounted on a 1.5m radius arc with a minimum angular separation of 10° between two adjacent housings, and each housing is equipped with a rod that allows the distance of the microphone from the centre of the arc to be adjusted. Each microphone is positioned 1.3m from the centre of the propeller. Figures 4.5 and 4.6 show in detail the set up used to make the acoustic measurements.
Microphone signals are recorded for a total of 120 s at 51.2 kHz. The acoustic measurements were conducted for two cases: with and without the propeller. The acoustic acquisitions without the rotor were made to assess what the background noise level was due to the presence of the grid.

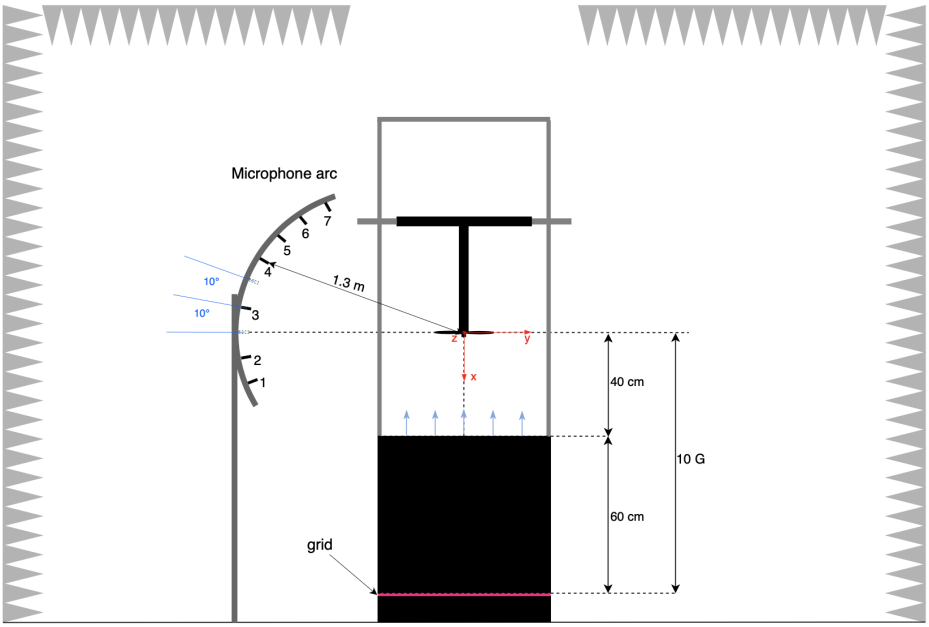

Figure 4.5: Schematic representation of the acoustic setup.

4.4 PIV measurements

The flow is seeded with particles of 1 µm generated by a SAFEX Twin Fog generator, with SAFEX-Inside-Nebelfluid. The field of view is illuminated using a Quantel Evergreen EVG00200 Nd:YAG laser, which has a double cavity and delivers 200 mJ of energy per pulse and with a maximum repetition rate of 15 Hz. Two different stereoscopic PIV configurations were implemented to study the flow, which are described in detail below.

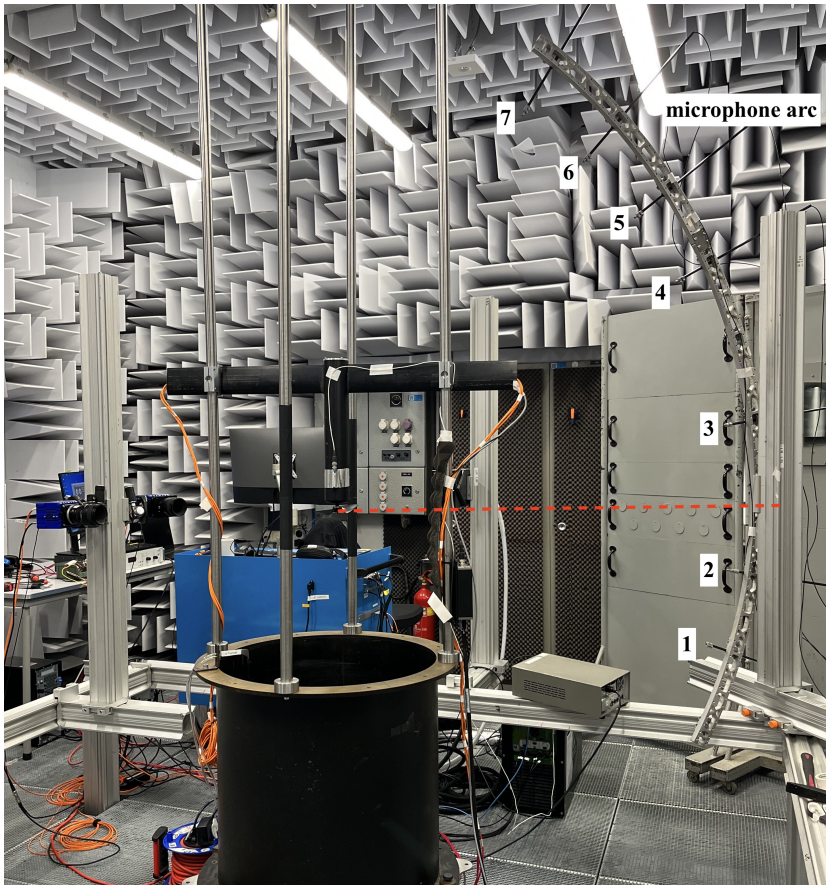

Figure 4.6: Microphone arc mounted in the A-tunnel.

4.4.1 Inflow Stereo PIV

Stereo PIV measurements have been conducted to study the inflow of the propeller. The set-up is shown in figure 4.7. In order to capture the images of the illuminated particles two LaVision sCMOS cameras with 2560 $\times$ 2160 pixels were used. Each camera was equipped with an AF Micro Nikkor lenses with 105 mm focal length. The lenses are operated ad a $f_{\#}$ of 11. In order to ensure a uniform focusing on the measurement plane, one of the two cameras (Camera 2) was equipped with a Scheimpflug adapter. Acquisitions were made both with and without propeller. Moreover, in the case with the propeller the acquisitions were made both sampling statistically uncorrelated snapshots, as well as phase-locked snapshots. In order to achieve synchronized measurements, a trigger signal from the encoder installed on the motor shaft was employed to regulate the timing of both the laser and the camera. By setting a trigger delay within the software, images were captured precisely when the blade was in alignment with the laser plane. The LaVision Davis 10.2 software was utilized to perform cameras calibration, acquisition, and post-processing of the particles' images.

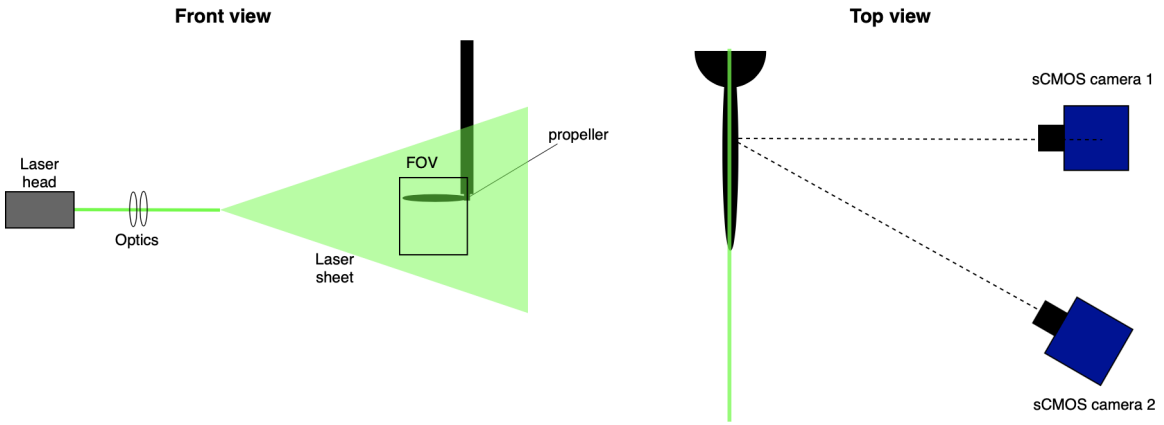

Figure 4.7: Inflow stereo PIV set-up.

4.4.2 Leading edge Stereo PIV

A different set-up was built to study the flow over the cross section of the blade, with particular focus on the flow field near the leading edge, at three different span-wise positions r/R of 25%, 50% and 75%. To allow for a full illumination of the flow field, a beam splitter and a sequence of mirrors were employed to divide the laser beam emerging from the laser head, as shown in figure 4.8. The laser beam was effectively split into two distinct laser paths thus allowing for the illumination of the blade from either sides. In order to capture the images of the illuminated particles two LaVision sCMOS cameras with 2560 $\times$ 2160 pixels were used. Each camera was equipped with an AF Micro Nikkor lenses with 105 mm focal length. The lenses are operated ad a $f_{\#}$ of 11. In order to ensure a uniform focusing on the measurement plane, the two cameras were equipped with Scheimpflug adapters. Also in this case the encoder signal was used to perform phase-locked measurements. Furthermore, also here the LaVision Davis 10.2 software was utilized for performing camera calibration, acquisition, and post-processing.

4.5 Oil-flow visualization

Surface oil-flow visualization was conducted to observe the flow patterns on the propeller blade. A fluorescent mixture, derived from 50 mL of liquid-paraffin wax and 20 drops of fluorescent oil additive A-680, was applied to the propeller surface. The propeller was adjusted to the desired operating conditions and was operated for about 5 minutes, allowing the paraffin to spread across the surface and attain its final configuration. The propeller was then gradually brought to a stop. While the propeller was at rest, an ultraviolet lamp with a wide aperture was used to illuminate it, and images were captured by taking snapshots of the blade surface.

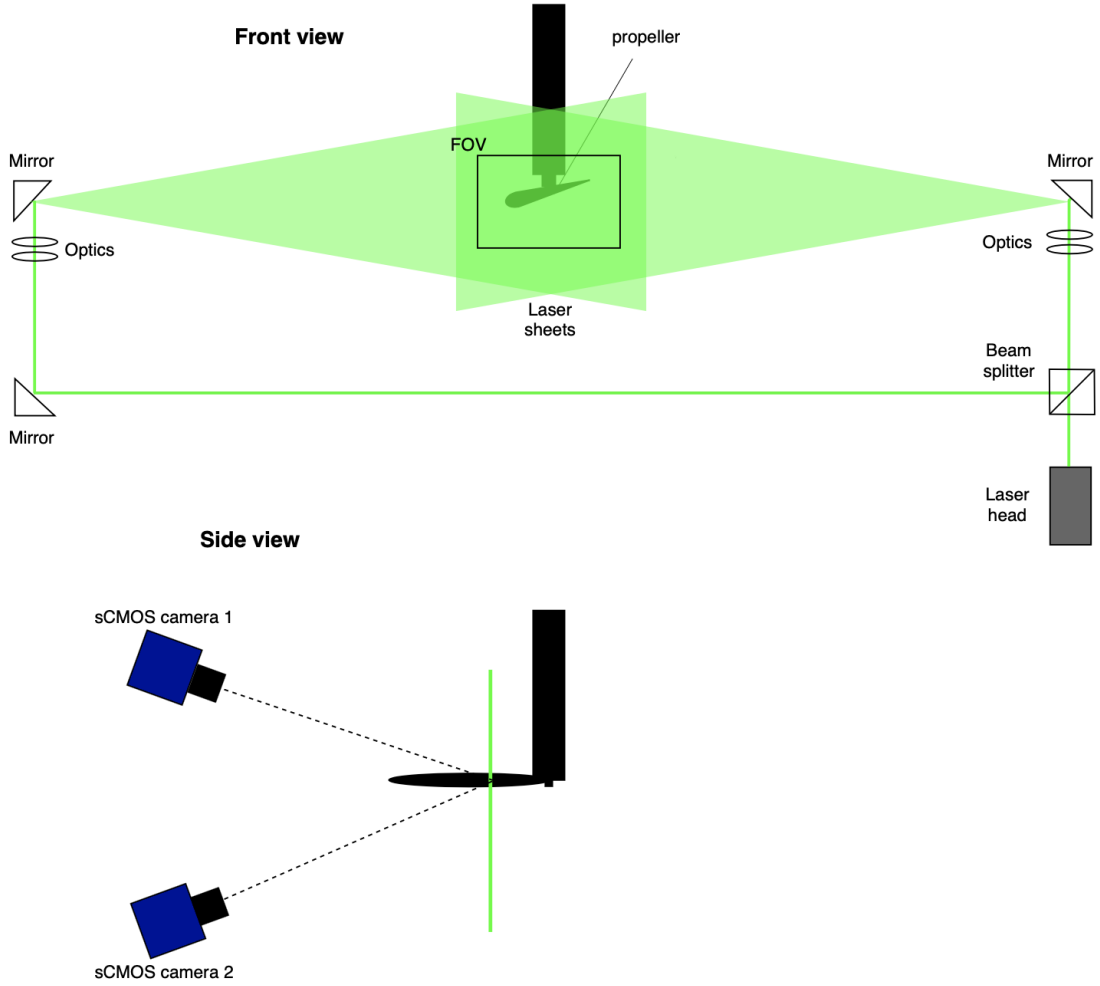

Figure 4.8: Leading edge stereo PIV set-up.

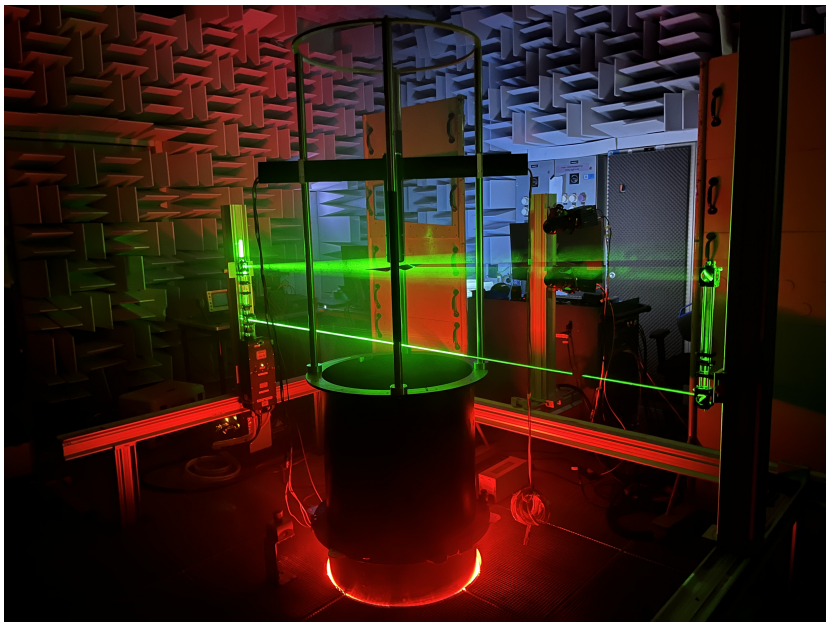

Figure 4.9: Leading edge stereo PIV set-up mounted in the A-Tunnel.

5

Experimental results

In this chapter, the experimental results are presented and discussed. First of all, the impending flow is characterized by analysing the case without the propeller in order to understand the characteristics of the grid generated turbulence. Next, a comparison is made between the case without the propeller and the case with the propeller to analyse how the presence of the latter changes the flow characteristics.

5.1 Flow characterization

In this section the flow will be characterized in terms of its statistical properties. From now on, a reference system will be considered which is slightly different from the one considered so far and which is highlighted in figure 5.1. In this new reference system, whose centre coincides with the centre of the propeller, the negative x-coordinate indicates a flow region upstream the propeller, while a positive x-coordinate indicates a flow region downstream the propeller.

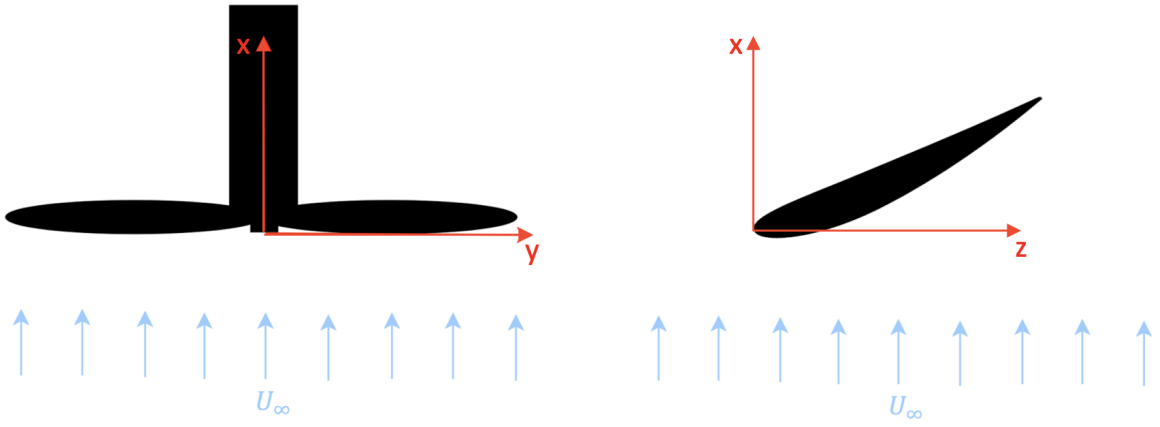

Figure 5.1: New coordinate system.

Figure 5.2 shows the colormap of the time-averaged streamwise velocity component, of the three analysed cases: (a) without the propeller, (b) with the propeller, statistically uncorrelated data, (c) with the propeller, phase-locked data.

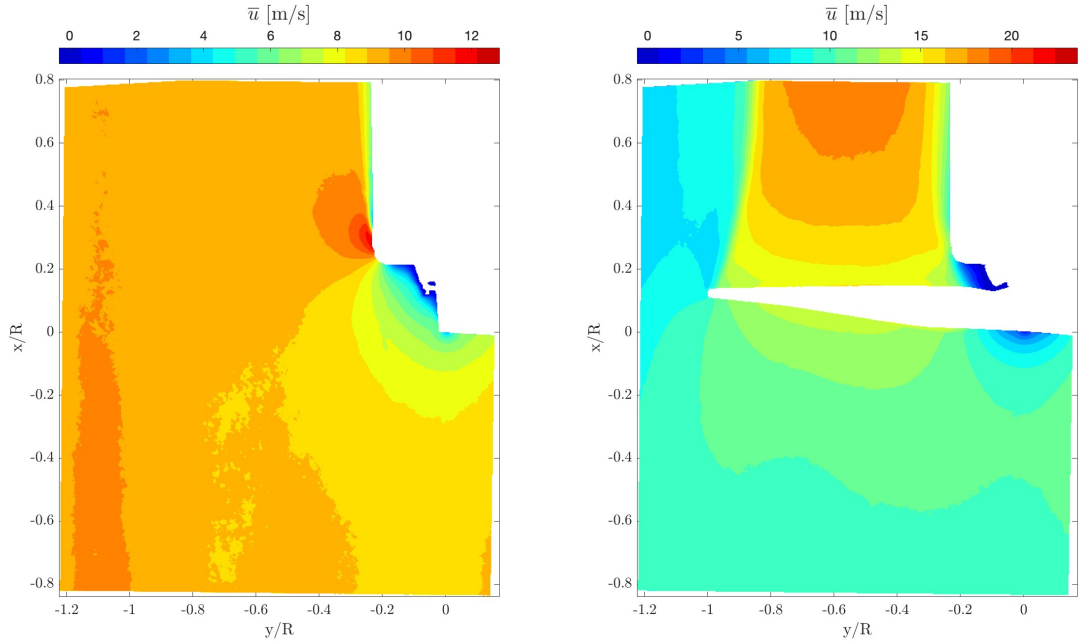

(a) Prop Off

(b) Prop On - Uncorrelated

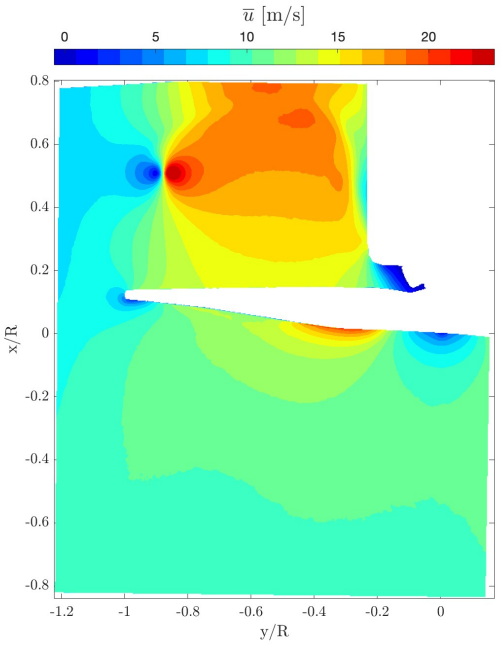

(c) Prop On - Phase-locked

Figure 5.2: Colormap of the time-averaged streamwise velocity component $\overline{u}$, for the three analysed cases: (a) without the propeller; (b) with the propeller, statistically uncorrelated data; (c) with the propeller, phase-locked data.

5.1.1 Impending turbulent flow characterization

First, the PIV and hot-wire anemometry data for the non-propeller case are considered to analyse the characteristics of the incoming turbulent flow.

Turbulence intensity

To assess the streamwise and normal components of turbulence intensity, PIV data of the standard deviation of these two velocity components were considered. For simplicity, we consider the evolution of these quantities in two cases: at fixed upstream distances $x = [7, 50, 100]$ mm and at certain fixed spanwise sections $r/R = 1.00, 0.75$ and 0.50, as shown in figure 5.3.

Figure 5.4 shows the values of the standard deviation of the streamwise and the radial

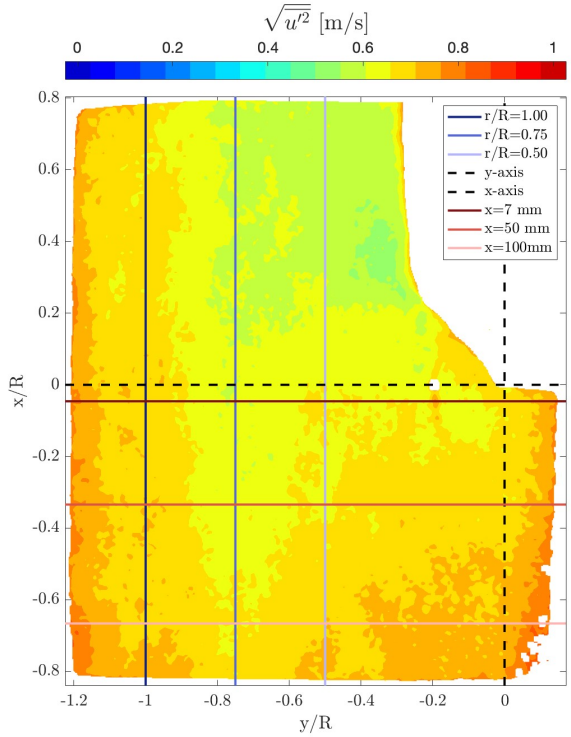

Figure 5.3: Standard deviation of the streamwise velocity component, $\sqrt{u'^2}$. Fixed upstream positions (red lines) and spanwise positions (blue lines) that will be considered.

velocity components, normalized with respect to U_∞ and compares their trends with those predicted by Roach for the decay of turbulence intensity downstream of a grid (see equations 2.13). The blue lines refer to PIV data for constant spanwise sections of $r/R = 1.00, 0.75$ and 0.50. The values from the hot-wire data (HW) were obtained by averaging all radial values at a fixed upstream distance. As it can be seen from the plots, both components appear to follow the trend predicted by Roach quite closely, and there is a good agreement between the PIV data and the hot-wire anemometry data. Only for positive x-coordinates is it noticeable that the experimental data de-

viate slightly from the theoretical trend predicted by Roach. This can be explained by the fact that in the case analysed, the propeller is not present, but the hub is, and since its size is not negligible, this element disturbs the flow.
On the other hand, the red lines in figure 5.5 show the evolution of the values of the standard deviation of the streamwise (a) and the radial (b) velocity components normalized with respect to U_∞ for different constant upstream positions $x = [7, 50, 100]$ mm as the radial position changes. In addition, the hot-wire data were obtained by averaging all upstream values at a fixed spanwise section. Again, there is good agreement between the PIV data and the hot-wire anemometry data. It is important to notice that there is a difference in the statistics along the radial positions, particularly for the radial velocity component. This indicates that the upstream turbulence field is not perfectly homogeneous.

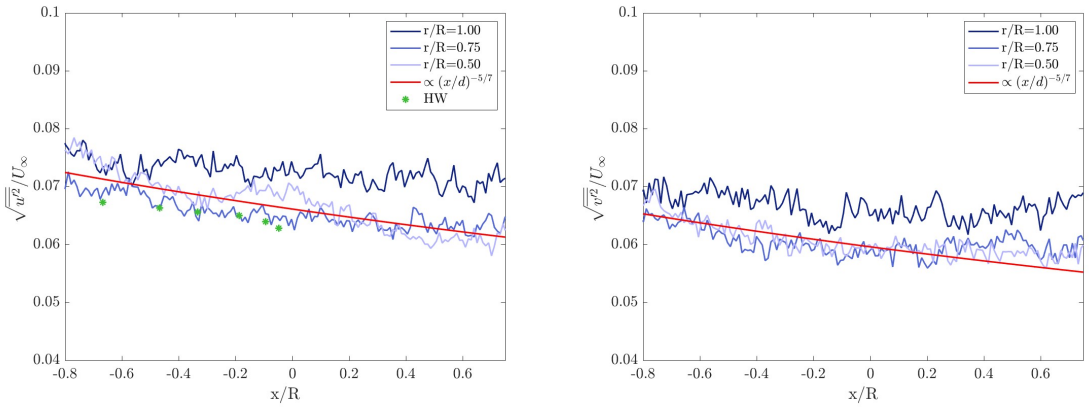

(a) Streamwise component (b) Radial component

Figure 5.4: Standard deviation of the streamwise and the radial velocity components at fixed spanwise positions, normalized with respect to U_∞. Comparison with the trend predicted by Roach.

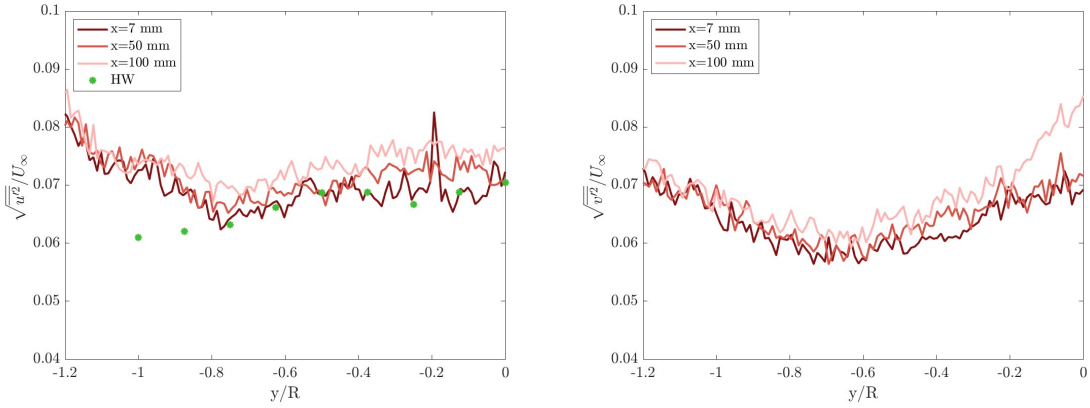

(a) Streamwise component (b) Radial component

Figure 5.5: Standard deviation of the streamwise and the radial velocity components at fixed upstream positions, normalized with respect to U_∞.

Integral length scale

In addition to turbulence intensity, the other important characteristic of turbulence to assess is the integral length scale, using hot-wire anemometry data from the case without the propeller. Considering a fixed upstream position of x =100 mm, figure 5.6 shows the turbulence spectra for different radial positions.

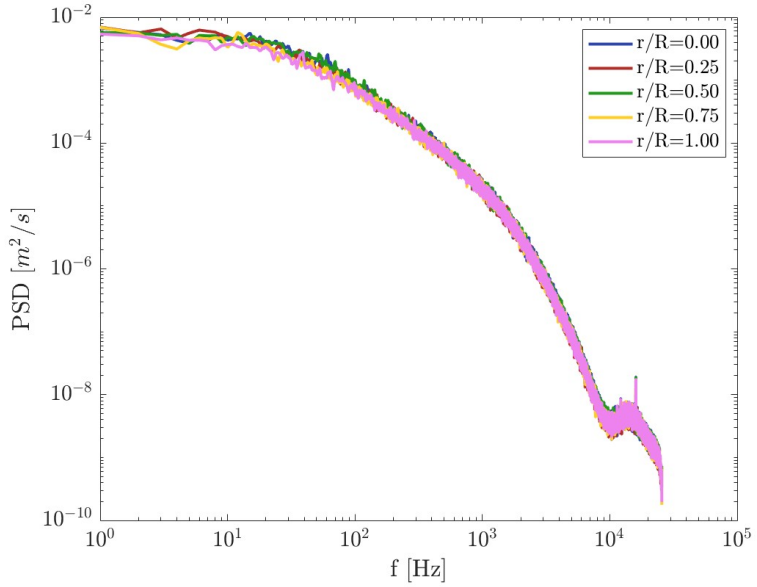

Figure 5.6: One-dimension turbulent velocity spectra for different radial positions and fixed upstream distance x =100 mm, obtained from hot-wire data.

From these data an evaluation of the integral length scales can be made. This is done applying the following formula proposed by Pope [24]:

$$L_{uu} = \frac{\pi E_{uu}(0)}{2\langle u^2 \rangle} = \frac{\pi PSD_{f=1}}{2\langle u^2 \rangle} \tag{5.1}$$

The results are tabulated in table 5.1. It is possible to notice a difference in the statistics along the radial positions, indicating that the upstream turbulence field is not perfectly homogeneous. The table also shows the mean value of the length scale evaluated from the experimental data and the value predicted by Roach (see equation 2.16), and it can be seen that the two values are quite similar.

r/R	0.00	0.25	0.50	0.75	1.00	$\overline{\mathbf{L_{uu}}}$ [m]	$\mathbf{L_{Roach}}$ [m]
$\mathbf{L_{uu}}$ [m]	0.015	0.023	0.014	0.020	0.012	0.017	0.019

Table 5.1: Integral length scale evaluated at x=100 mm upstream the propeller, for different spanwise positions. Mean value and comparison with Roach prediction.

5.1.2 Effect of the propeller

The next step is to analyse how the presence of the propeller influences the flow field.

Streamtube contraction

As can be seen from figure 5.2(b), the presence of the propeller causes the flow to accelerate. This leads to the contraction of the streamtube, with an effect similar to that described in section 2.3.1 . Since the contraction is not geometrical, but due to the fact that the flow is accelerating, we want to calculate the contraction ratio (CR). Referring to the figure below, we can say that in the investigated case we have:

$$CR = \frac{U_2}{U_1} = \frac{\overline{u}_{(x/R=0.7)}}{\overline{u}_{(x/R=-0.8)}} \approx 1.82. \tag{5.2}$$

The kink in the plot (black line) is due to the presence of the reflection associated with the passage of the blade.
In the previously discussed paper [31] the minimum contraction ratio analysed was equal to 4, while in this case CR is less then half. This leads us to hypothesise that the turbulence distortion phenomenon due to streamtube contraction may be less pronounced than in the previously seen cases.

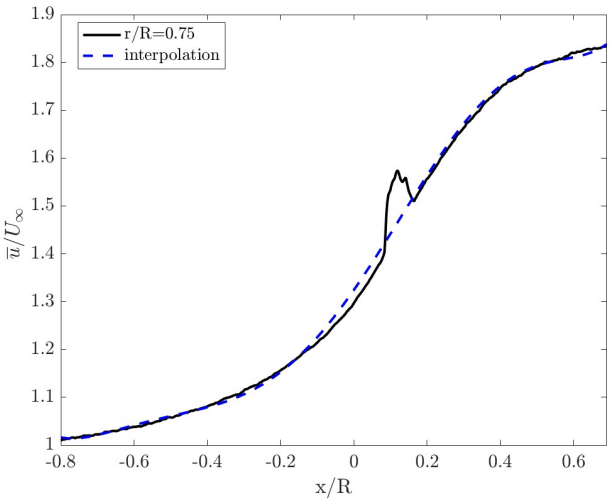

Figure 5.7: Streamtube contraction.

Turbulence distortion

This section proposes an analysis of turbulence intensity similar to that shown in section 5.1.1, but comparing the case without the propeller (Prop Off case) and the case with the propeller (Prop On case). This is done in order to understand how the presence of the rotor affects the turbulence intensity. In particular, for the Prop On case, two different sets of images were considered: an uncorrelated one and a phase-locked one. In this second case, the blade is positioned across the light sheet, i.e. in the PIV acquisition plane. Instead, in the case of uncorrelated acquisition, for each PIV image

considered, the y-direction of the blade creates an angle with respect to the acquisition plane that is different from that of the previous image. Therefore, the uncorrelated case will give us an idea of the general effect of the blade on the motion field, while the phase-locked case will highlight the case where the presence of the blade affects the most the flow field. Figures 5.8 and 5.9 show the standard deviations of the streamwise and radial velocity components for the three cases described.

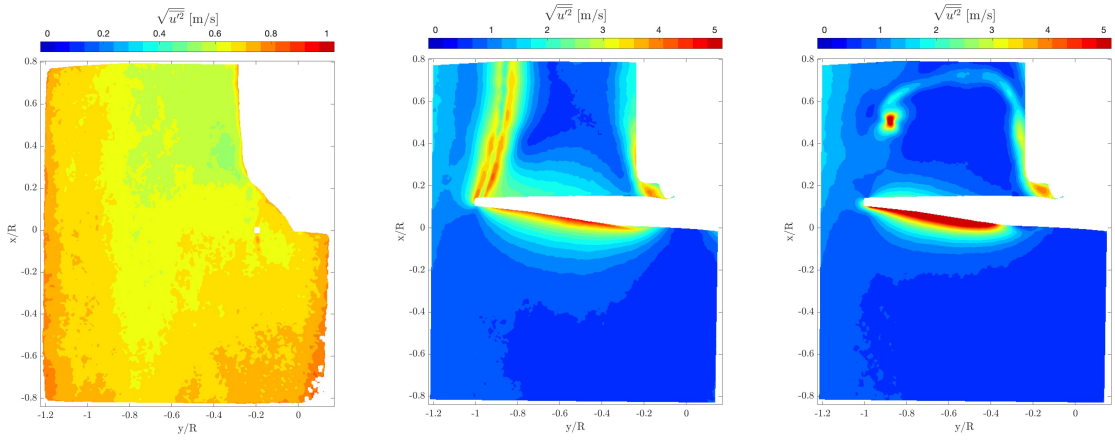

(a) (b) (c)

Figure 5.8: Standard deviation of the streamwise velocity component for the three different analyzed cases: (a) Prop Off, (b)Prop On - Uncorrelated, (c) Prop On - PL.

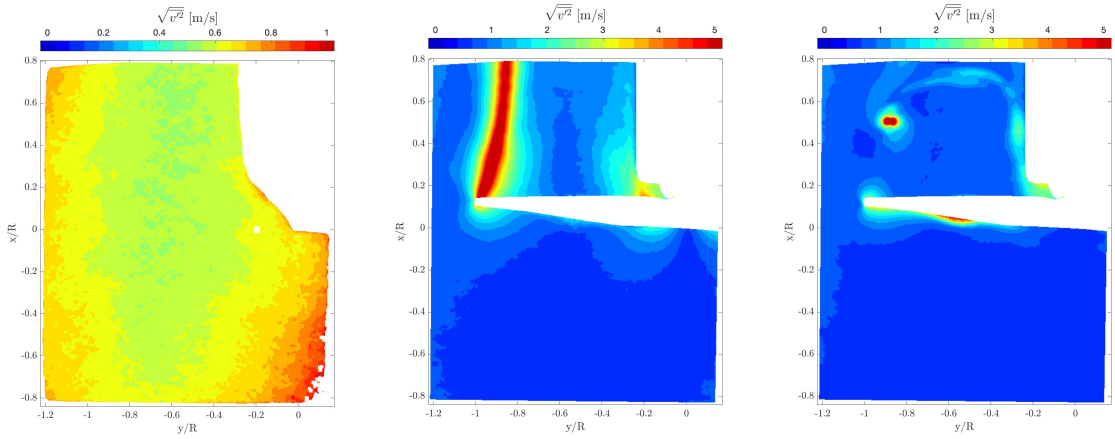

(a) (b) (c)

Figure 5.9: Standard deviation of the radial velocity component for the three different analyzed cases: (a) Prop Off, (b)Prop On - Uncorrelated, (c) Prop On - PL.

Figure 5.10 shows the values of the standard deviation of the streamwise (a) and radial (b) velocity components, normalized with respect to U_∞, in the three different cases

just described, for a fixed spanwise section of $r/R = 0.75$. Figure 5.11 shows the same quantities for the same three cases, but for different fixed upstream positions $x = [7, 50, 100]$ mm. In the region far upstream the propeller, there is little difference between the case with propeller and the case without propeller, so it is possible to say that the statistical characteristics of the upstream turbulence are preserved for the two cases analysed. As one approaches the rotor plane, it can be seen that both the quantities increase. This is partly due to the effect of streamtube contraction and partly due to the turbulence distortion near the leading edge. There may also be spurious effects due to blade rotation and reflections. Due to the physics of the problem and the way the data were collected, it is not possible to decouple these effects and determine which is dominant.

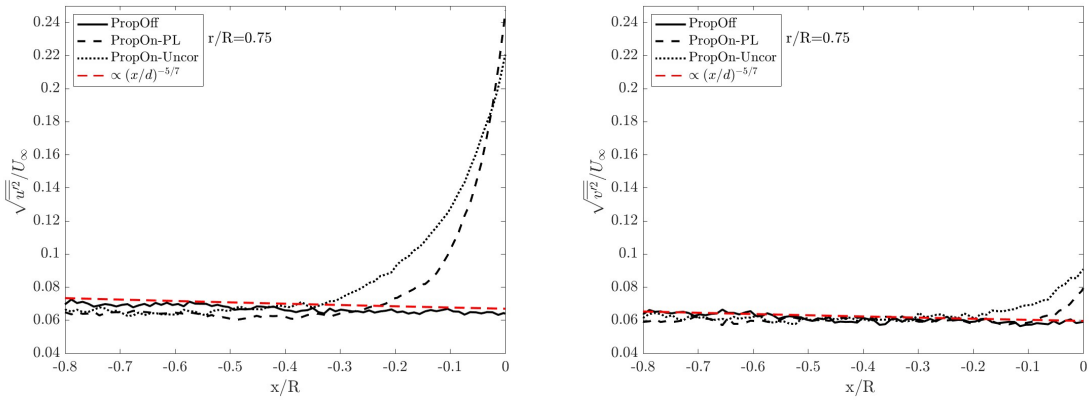

(a) Streamwise component

(b) Radial component

Figure 5.10: Standard deviation of the streamwise and the radial velocity components, normalized with respect to U_∞, at $r/R = 0.75$. Comparison between the three different analyzed cases and the trend predicted by Roach.

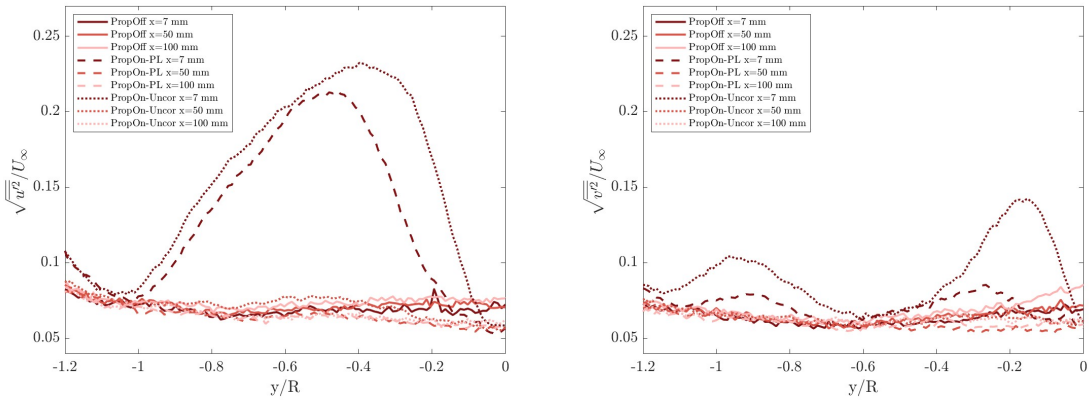

(a) Streamwise component

(b) Radial component

Figure 5.11: Standard deviation of the streamwise and the radial velocity components, normalized with respect to U_∞, at different fixed upstream positions. Comparison between the three different analyzed cases.

Phase-locked leading edge PIV

In this section we will try to better understand what is happening with the turbulence intensity near the leading edge. Therefore, we will consider the images obtained with the second PIV setup, consisting of phase-locked images of the flow field near the leading edge, for 3 different spanwise positions $r/R = 0.25$, 0.50 and 0.75. These data allow us to determine the turbulence intensity for positions very close to the blade. As before, we consider the standard deviation of the streamwise and normal (along the chord) velocity components, normalized with respect to U_∞ at two different distances from the blade leading edge: one as close as possible to the leading edge and one at a distance upstream $x/c_{section} = 1$.
Although the image acquisition is phase-locked, the blade will not always be in exactly the same position during the acquisition due to a slight RPM variation. This leads to an increase in the standard deviation close to the blade, but does not represent the physical situation. There are also laser reflections in the same area. In order to minimise the difference in blade position between images and to maintain confidence in the flow statistics, a subset of images is processed in which the blade maintains approximately the same position. Due to the two effects just described (reflections and RPM variability), the measurements near the blade are corrupted, as can be seen from the figures 5.12, 5.14, 5.16. The green line therefore represents the first upstream position relative to the blade where the standard deviation is considered to be correct and representative of the physical phenomenon studied.
Figures 5.13, 5.15 and 5.17 show the values of the standard deviation of the streamwise and the normal (chord-along) velocity components, normalized with respect to U_∞ at three different spanwise position and for two different distances upstream the leading edge. Firstly, the values away from the leading edge are similar for the two distances considered and show good agreement with the values obtained from the inflow PIV data analysis previously seen for the cases at r/R =0.50 and 0.75. The case related to the section r/R =0.25 presents a range of lower values: this could be due to the fact that the section considered is very close to the hub, which creates a significant blocking effect. Focusing on the streamwise component, we can see that the described quantity increases as we get closer to the leading edge. Also, considering the radial distribution of this increase it seems that this effect intensifies as we move toward the blade tip. Since the displayed field of view is very small and the focus is precisely on the area close to the leading edge of the blade, we can say that this increase is due to the turbulent distortion mechanism caused by the interaction of the turbulent flow with the profile.

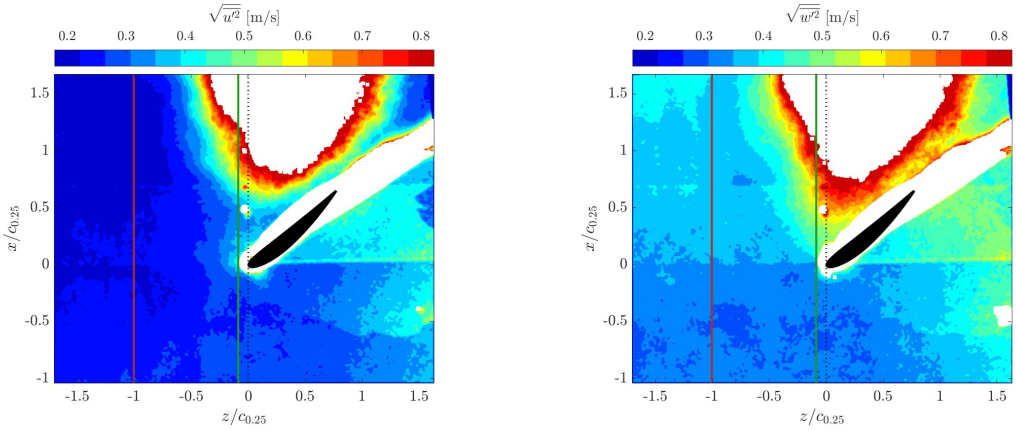

(a) Streamwise component (b) Chord-wise component

Figure 5.12: Standard deviation of the streamwise and chord-wise velocity components at $r/R = 0.25$.

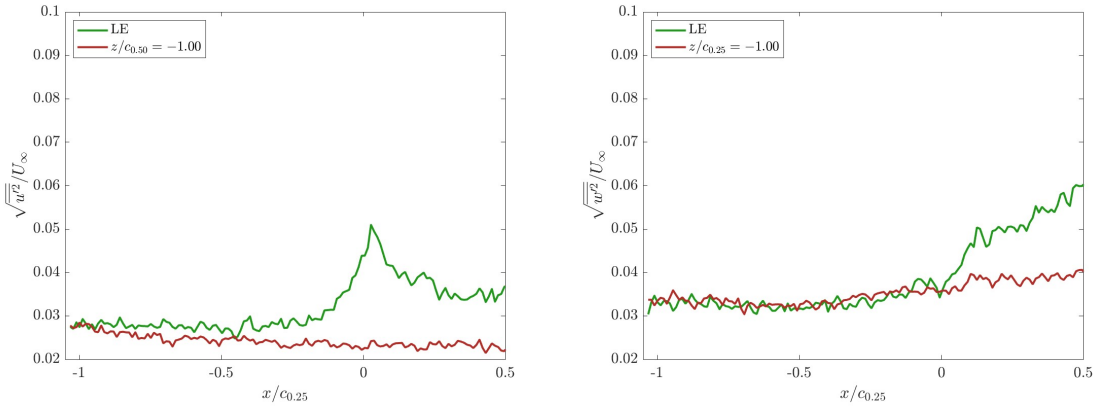

(a) Streamwise component (b) Chord-wise component

Figure 5.13: Standard deviation of the streamwise (a) and the chord-wise (b) velocity components, normalized with respect to U_∞, at $r/R = 0.25$ and at different distances from the leading edge.

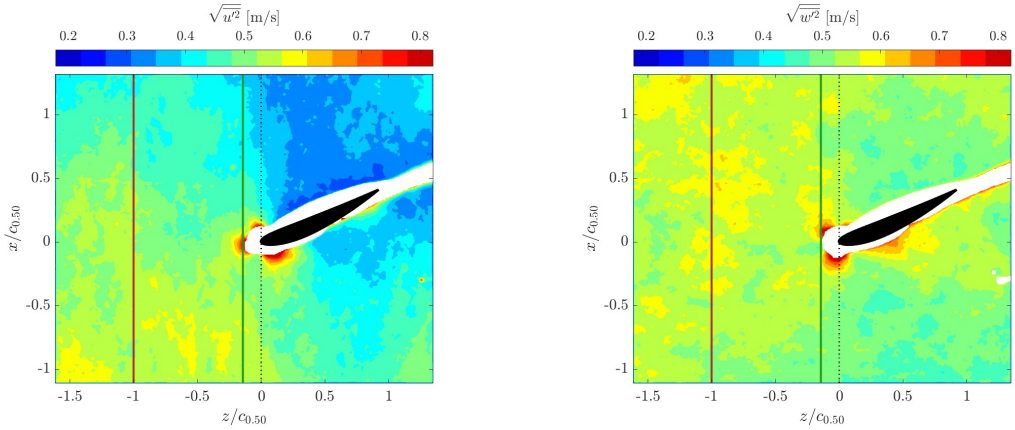

(a) Streamwise component (b) Chord-wise component

Figure 5.14: Standard deviation of the streamwise and chord-wise velocity components at $r/R = 0.50$.

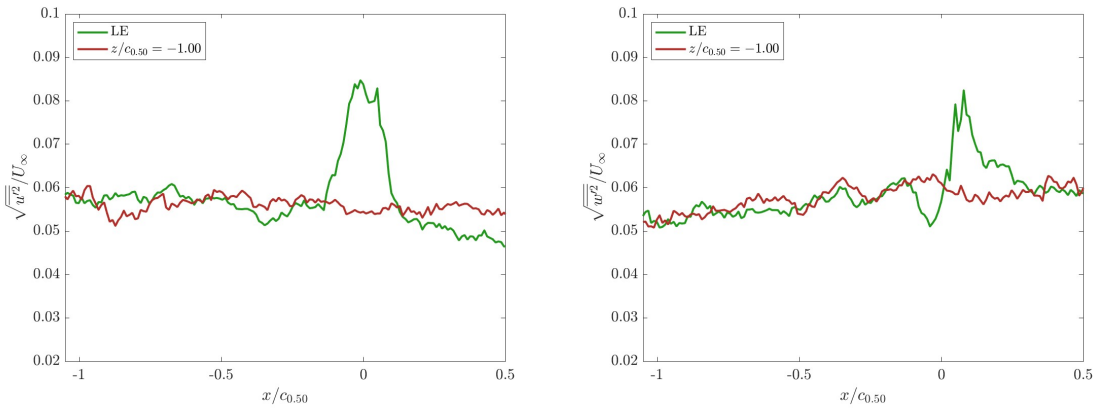

(a) Streamwise component (b) Chord-wise component

Figure 5.15: Standard deviation of the streamwise (a) and the chord-wise (b) velocity components, normalized with respect to U_∞, at $r/R = 0.50$ and at different distances from the leading edge.

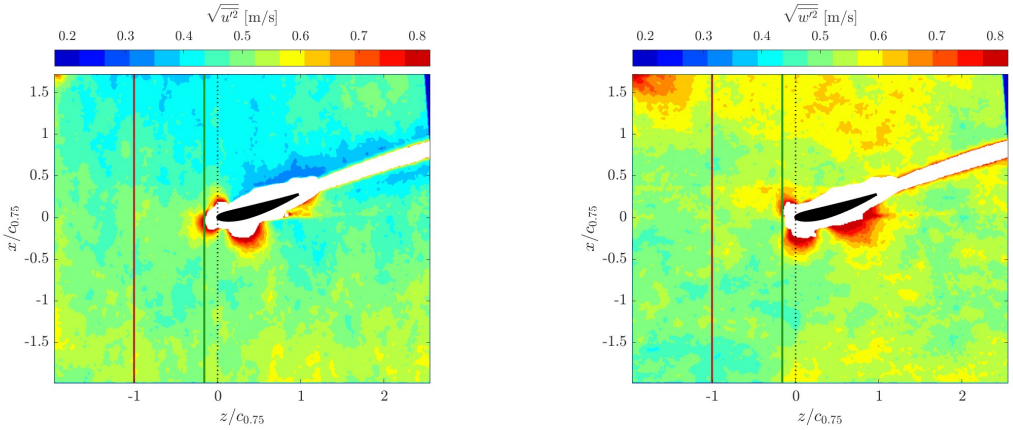

(a) Streamwise component (b) Chord-wise component

Figure 5.16: Standard deviation of the streamwise and chord-wise velocity components at $r/R = 0.75$.

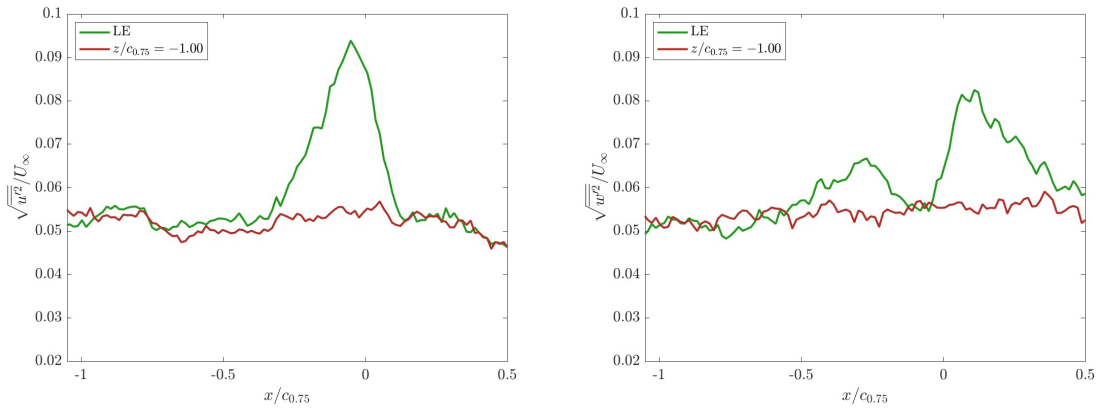

(a) Streamwise component (b) Chord-wise component

Figure 5.17: Standard deviation of the streamwise (a) and the chord-wise (b) velocity components, normalized with respect to U_∞, at $r/R = 0.75$ and at different distances from the leading edge.

5.2 Laminar separation bubble

Another interesting thing to investigate is whether or not the laminar separation bubble (LSB) is present under the operating conditions considered. Figure 5.18 shows the oil-flow visualization of the suction side of the propeller blade. The way the oil spreads on the blade surface clearly indicates a laminar separation bubble is present. The oil layer appears thicker in parts of the blade where the pressure gradient along its length is almost zero, like in the LSB, and in areas where the airflow simply separates, such as at the root. The laminar separation bubble, in the figure below, is the area between the laminar separation line (denoted by S) and the reattachment line (denoted by R).

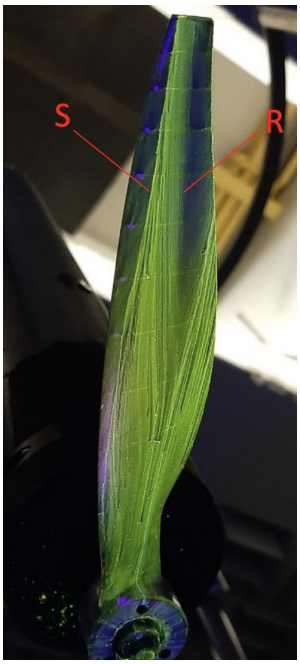

Figure 5.18: Oil-flow visualization of the suction side of the blade.

5.3 Acoustics

This section examines the acoustic data. First, an assessment of the background noise is made and then a comparison is made between the experimental acoustic data and the noise level predicted by the analytical model.

5.3.1 Background and motor noise

Before analysing propeller noise, it is important to remember that there are other noise-producing elements that will add to the noise produced by the propeller and affect the results. For this reason an analysis of the background and motor noise is conducted. The noise radiation is investigated in terms of sound power level (PWL). The PWL is computed with the expression used by Narayanan *et al.* [20] in their experimental campaign, reported hereafter:

$$PWL(f) = 10\log_{10}\Big(\frac{S_W(f)}{W_{ref}}\Big) \tag{5.3}$$

where $W_{ref} = 10^{-12}\,\mathrm{W}$ and $S_W(f)$ is the spectral density of the sound power radiated between the radiation angles $[\theta_{mic_1} : \theta_{mic_7}]$. Its expression is the following:

$$S_W(f) = \Big(\frac{LR}{\rho_0 c_0}\Big)\Bigg\{\sum_{i=1}^{N-1}\Big(\frac{S_{PP}(\theta_i) + S_{PP}(\theta_{i+1})}{2}\Big)\Delta\theta\Bigg\} \tag{5.4}$$

where $S_{PP}(\theta_i)$ is the acoustic pressure PSD (power spectral density) measured at measurement angle θ_i and N is the number of microphones, L =0.3 m is the span of the propeller, R =1.3 m is radius of the microphone arc, $\Delta\theta$ is angle between two adjacent microphones, ρ_0 is the air density and c_0 is the speed of sound.
In figure 5.19 the overall noise produced by the propeller has been compared with the noise of the grid only and the noise produced by the grid and the motor. The frequency axis of is normalized with respect to the the blade passing frequency:

$$BPF = \frac{nt}{60} = 200\,\mathrm{Hz} \tag{5.5}$$

where $n = 2$ is the number of blades and t is the rotation velocity (6000 rpm).
The noise generated by the combined effect of the grid and the electric motor has a series of discrete tones in the range BPF 2-BPF 50. Its broadband level does not affect the noise measurements either, being at a different level with respect to the propeller noise over the whole frequency range in all cases except the interval BPF 6- BPF 30. Finally, an additional source of tonal noise in the experiment is the vibration of the test rig and the rotor.

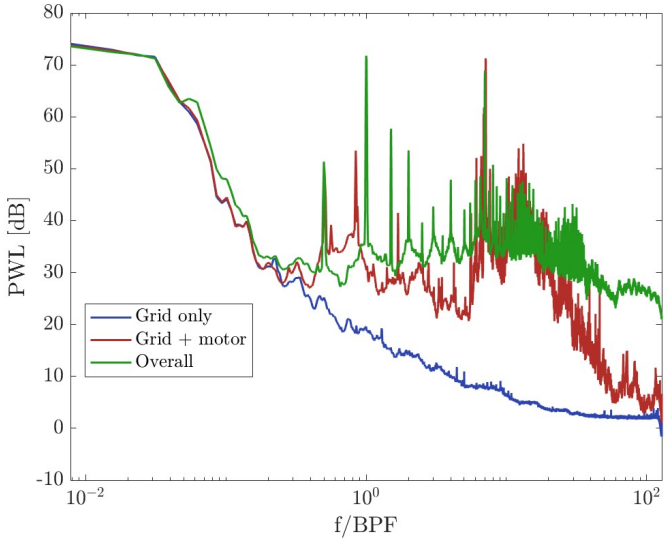

Figure 5.19: Comparison between propeller noise and background/motor noise.

5.3.2 Predictive model

In this part, a comparison is made between the experimental data and the noise predicted by the model. In particular, the input data to the model are the turbulence intensity and the integral length scale values of the free stream turbulence, evaluated at x=100mm upstream of the propeller and the number of strips considered is $N_{strip} = 8$. Figure 5.20 shows the comparison between the predicted noise and the experimental data in terms of sound pressure level (SPL) for the microphones 1, 3, 5 and 7, where:

$$SPL(i) = 10 \log_{10} \left(\frac{PSD(i)}{p_{ref}^2} \right) \tag{5.6}$$

where i is the index of the microphone, $PSD(i)$ is the power spectral density of that microphone, and $p_{ref} = 2 \cdot 10^{-5}$ Pa.
For microphones placed at small angles to the plane of rotation of the propeller (such as microphones 1 and 3), a greater difference between the experimentally measured noise and the prediction curve can be seen, and thus a lower accuracy of the model. On the other hand, for microphones placed at larger angles (such as microphones 5 and 7), the prediction is more accurate. This difference in accuracy depending on the position of the microphone relative to the propeller plane could be due to the fact that to implement the inverse stripe theory, the simplified Amiet model has to be applied, which is only valid in the midspan plane of the blade. This effect is then reflected in the comparisons between the noise predicted by the model and the noise measured experimentally in terms of PWL, shown in figure 5.21, which takes all microphones into account.

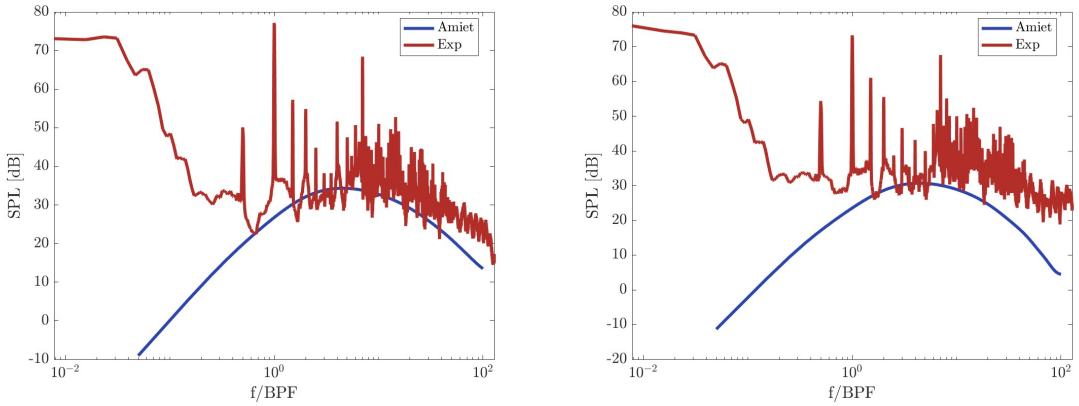

(a) Mic 1

(b) Mic 3

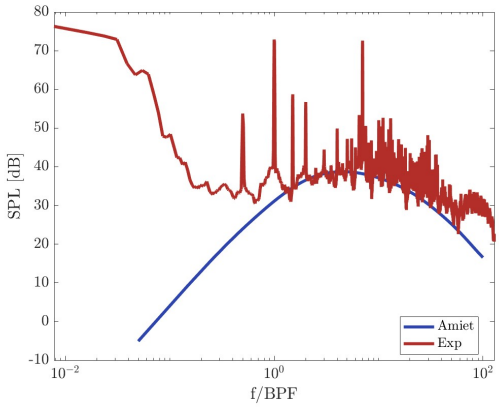

(c) Mic 5

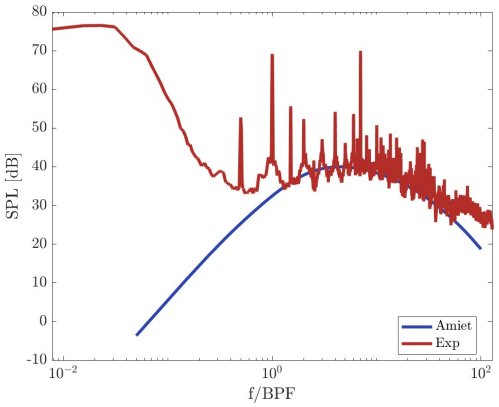

(d) Mic 7

Figure 5.20: Experimental and predicted noise spectra for microphones 1, 3, 5 and 7.

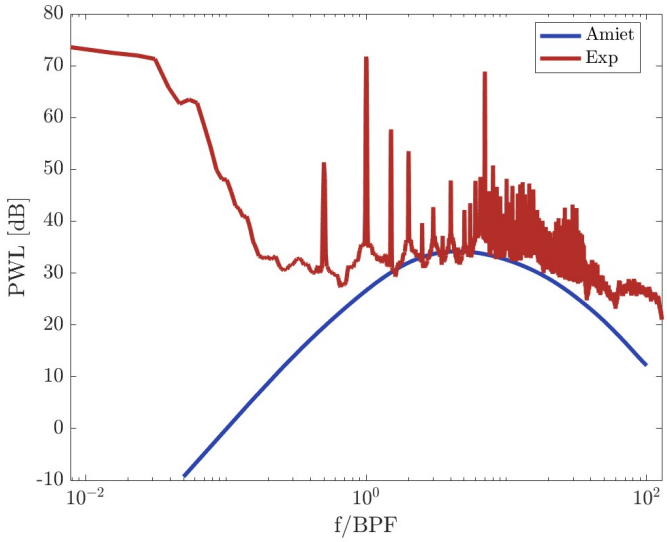

Figure 5.21: Experimental and predicted noise PWL.

6

Conclusions

UAVs have demonstrated immense versatility, but the considerable noise generated by their propellers remains a major obstacle, especially if we aim for their integration into everyday environments. The aim of this work was to improve our understanding of how turbulence affects the aeroacoustics of small propellers operating at low Reynolds number, with the aim of understand better which are the characteristics of their noise emissions.

This investigation began by studying the behaviour of turbulence when it interacts with a grid. By comparing experimental data with theoretical predictions, we found that existing formulae accurately described the decay of turbulence downstream of a grid. This initial analysis provided a solid foundation for understanding the dynamics of turbulence, which is crucial for assessing its impact on propeller noise.

Then, the effects of introducing a propeller into a turbulent flow have been studied. This investigation revealed changes in turbulence characteristics, in particular turbulence intensity. However, determining the dominant influence between the streamtube contraction due to flow acceleration and the distortion of the turbulence caused by the propeller proved challenging. The complexity of the data underlines the intricate relationship between these two phenomena that can not be decoupled.

We then looked at the noise generated by the propeller under fixed operating conditions. Using turbulence statistics, propeller geometry data and flow information, a modified version of Amiet's propeller turbulence absorption noise model has been developed. This model provides predictions of the power spectral density of the broadband noise emitted by the propeller in the far field, accounting for spanwise variations through inverse strip theory. However, this approach is not without limitations. Assumptions regarding the homogeneity and isotropy of the turbulence may not always hold true, and the applicability of the simplified Amiet model, which is restricted to the midspan plane of the blade, presents challenges in accurately modelling propeller noise.

In conclusion, this thesis contributes to our understanding of the complex interplay between turbulence and propeller noise in UAVs. By elucidating these relationships, we aim to develop strategies to reduce propeller noise, thereby increasing the usability and acceptance of UAVs in various domains.

Bibliography

[1] R.K. Amiet. "Noise produced by turbulent flow into a rotor: theory manual for noise calculation". In: *NASA Contractor report 181788* (1989).

[2] R.K.. Amiet. "Acoustic radiation from an airfoil in a turbulent stream". In: *Journal of Sound and Vibration* 41 (1975), pp. 407–420.

[3] K.S. Aravamudan and W.L. Harris. "Low-frequency broadband noise generated by a model rotor". In: *The Journal of the Acoustical Society of America* (1979).

[4] C. Bailly and G. Comte-Bellot. *Turbulence*. Springer, 2015.

[5] M. S. Boutilier and S. Yarusevych. "Parametric study of separation and transition characteristics over an airfoil at low Reynolds numbers". In: *Experiments in fluids* 52 (2012), pp. 1491–1506.

[6] P. Chaitanya et al. "Aerofoil geometry effects on turbulence interaction noise". In: *21st AIAA/CEAS aeroacoustics conference* (2015).

[7] A. W. Christian and R. Cabell. "Initial investigation into the psychoacoustic properties of small unmanned aerial system noise". In: *23rd AIAA/CEAS aeroacoustics conference* (2017).

[8] J. Christophe, J. Anthoine, and S. Moreau. "Amiet's theory in spanwise-varying flow conditions". In: *AIAA Journal* 47 (2009), pp. 788–790.

[9] P.A. Davidson. *Turbulence : An Introduction for Scientists and Engineers*. Oxford University Press, 2004.

[10] L.D. De Santana. "Analytical Methodologies for Airfoil Noise Prediction". PhD thesis. 2015.

[11] L.D. De Santana et al. "Rapid Distortion Theory modified turbulence spectra for semi-analytical airfoil noise prediction". In: *Journal of Sound and Vibration* 383 (2016), pp. 349–363.

[12] R.J. Garde. *Turbulent Flow*. 3rd Edition. New Academic Science, 2010.

[13] S. Glegg and W. Devenport. *Aeroacoustics of Low Mach Number Flows*. Elsevier, 2017.

[14] E. Grande et al. "Aeroacoustic investigation of a propeller operating at low Reynolds numbers". In: *American Institute of Aeronautics and Astronautics* 60.2 (2022), pp. 860–871.

[15] D.B. Hanson. "Spectrum of rotor noise caused by atmospheric turbulence". In: *The Journal of the Acoustical Society of America* (1974), pp. 407–420.

[16] J.C.R. Hunt. "A theory of turbulent flow round two-dimensional bluff bodies". In: *Journal of Fluid Mechanics* (1973), pp. 625–706.

[17] R.F. Miotto, W.R. Wolf, and L.D. de Santana. "Leading-Edge Noise Prediction of General Airfoil Profiles with Spanwise-Varying Inflow Conditions". In: *AIAA Journal* (2018), pp. 1711–1716.

[18] P.F Mish and W.J. Devenport. "An experimental investigation of unsteady surface pressure on an airfoil in turbulence—Part 2: Sources and prediction of mean loading effects". In: *Journal of Sound and Vibration* 296.3 (2006), pp. 447–460.

[19] S. Moreau and M. Roger. "Effect of angle of attack and airfoil shape on turbulence-interaction noise". In: *11th AIAA/CEAS aeroacoustics conference* (2005).

[20] S. Narayanan et al. "Airfoil noise reductions through leading edge serrations". In: *Physics of Fluids* 27 (2015).

[21] T. Ohtake, Y. Nakae, and T. Motohashi. "Nonlinearity of the Aerodynamic Characteristics of NACA0012 Aerofoil at Low Reynolds Numbers". In: *Japanese Society for Aeronautical and Space Science Papers* 55.644 (2007), pp. 439–445.

[22] R.W. Peterson and R.K. Amiet. "Noise of a model helicopter rotor due to ingestion of isotropic turbulence". In: *Journal of Sound and Vibration* (1982).

[23] A. Piccolo et al. "Impact of turbulence distortion on leading-edge noise generation and prediction".

[24] S.B. Pope. *Turbulent flows*. Cambridge university press, 2000.

[25] P.E. Roach. "The generation of nearly isotropic turbulence by means of grids". In: *International Journal of Heat and Fluid Flow* 8 (1987), pp. 82–92.

[26] F. L. dos Santos et al. "Modeling the turbulence spectrum dissipation range for leading-edge noise prediction". In: *American Institute of Aeronautics and Astronautics* (1982), pp. 3581–3592.

[27] F. L. dos Santos et al. "Modelling the dissipation range of von Karman turbulence spectrum". In: *American Institute of Aeronautics and Astronautics* (2021).

[28] R.H. Self. "Propeller noise". In: *Encyclopedia of Aerospace Engineering* (2021).

[29] M. Sevik. "Sound radiation from a subsonic rotor subjected to turbulence". In: *Fluid Mechanics, Acoustics, and Design of Turbomachinery* (1974).

[30] D.J. Tritton. *Physical Fluid Dynamics*. Oxford University Press, 1988.

[31] M.S. Uberoi. "Effect of Wind-Tunnel Contraction on Free-Stream Turbulence". In: *Journal of the Aeronautical Sciences* 23.8 (1956), pp. 754–764.

[32] L. Van Beek. *The distortion of turbulence by a low Reynolds number UAV propeller and the effect on aeroacoustics*. 2021.

[33] T. Von Karman. "Progress in the statistical theory of turbulence". In: *Proceedings of the National Academy of Sciences* 34 (1948), pp. 530–539.

[34] Q.R. Wald. "The aerodynamics of propellers". In: *Progress in Aerospace Science* 42 (2006), pp. 85–125.

[35] J. Winslow et al. “Basic understanding of airfoil characteristics at low Reynolds numbers ($10^4 - 10^5$).” In: *Journal of aircraft* 55.3 (2018), pp. 1050–1061.

[36] Y. Yauwenas et al. “The effect of inflow disturbance on drone propeller noise”. In: *25th AIAA/CEAS Aeroacoustics Conference* (2019).